Sizing the X-ray Spectral Resolution Limits of the REgolith X-ray Imaging Spectrometer (REXIS) Instrument at Asteroid 1999RQ36

By

Suzanna Megyery

Submitted to the Department of Earth, Atmospheric and Planetary Science
in Partial Fulfillment of the Requirements for the Degree of

BACHELOR OF SCIENCE
in Earth, Atmospheric and Planetary Sciences
at the

MASSACHUSETTS INSTITUTE OF TECHNOLOGY

January 17, 2013 [February 2013]

Signature of Author: Signature redacted

Suzanna Megyery
Department of Earth, Atmospheric and Planetary Sciences
January 17, 2013

Certified by: Signature redacted

Professor Sara Seager
Class of 1941 Professor of Planetary Sciences and Physics, Department of Earth, Atmospheric and Planetary Sciences
Thesis Supervisor

Accepted by: Signature redacted

Professor Richard P. Binzel
MacVicar Faculty Fellow, Professor of Planetary Sciences, Department of Earth, Atmospheric and Planetary Sciences
Chairman, Departmental Committee on Undergraduate Program

OSIRIS-REx Asteroid Sample Return Mission

NASA Goddard Space Flight Center
Lockheed Martin
University of Arizona
Massachusetts Institute of Technology
Harvard University

Massachusetts Institute of Technology

Department of Earth, Atmospheric & Planetary Sciences
Kavli Center for Astrophysics
Department of Aeronautics & Astronautics
Space Systems Laboratory

In Conjunction with: Harvard Center for Astrophysics

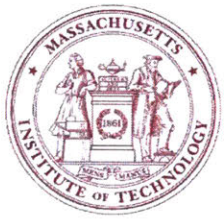

Sizing the X-ray Spectral Resolution Limits of the REgolith X-ray Imaging Spectrometer (REXIS) Instrument at Asteroid 1999RQ36

Submitted to the Department of Earth, Atmospheric and Planetary Science in Partial Fulfillment of the Requirements for the Degree of

BACHELOR OF SCIENCE

in Earth, Atmospheric and Planetary Science
at the

MASSACHUSETTS INSTITUTE OF TECHNOLOGY

Dated: 2013.01.17

Author:

Suzanna Megyery
zsuzsa@mit.edu

Massachusetts Institute of Technology
Department of Earth, Atmospheric & Planetary Sciences

Sizing the X-ray Spectral Resolution Limits of the REgolith X-ray Imaging Spectrometer (REXIS) Instrument at Asteroid 1999RQ36

By: Suzanna Megyery

Submitted to the Department of Earth, Atmospheric and Planetary Science
on January 17, 2013 in Partial Fulfillment of the Requirements for the
Degree of Bachelor of Science in Earth, Atmospheric and Planetary Science

Abstract

The REgolith X-ray Imaging Spectrometer (REXIS), a Charge-Coupled Device (CCD)-based coded aperture soft X-ray (0.3-7.5 keV) telescope for remote geochemical X-ray Fluorescence (XRF) spectrometry, will be flying on board the Origins Spectral Interpretations Resource Identification Security Regolith Explorer (OSIRIS-REx) asteroid sample return mission that will be visiting the asteroid 1999 RQ36 and sending a sample back to Earth. REXIS will detect elemental XRF lines and produce a histogram of results as the spacecraft orbits the asteroid as well as produce a global map of elemental abundance ratios. The accuracy requirement for measuring the global ratios of elements and the spectral resolution requirement for discriminating unique XRF lines from each other have been set in place.

The correct interpretation of X-ray measurements from the surface of 1999 RQ36 is limited by properties that are intrinsic to the CCD detector, CCID-41, that has been chosen for REXIS. This thesis study outlines student experimentation and results that were conducted on the CCID-41 detector to gauge the intrinsic detector noise as a function of detector temperature. Further, the widening of spectral lines on the resultant histogram was also equated as a function of detector temperature.

Members of the REXIS Team built a spectral resolution model to investigate both the widening of spectral lines as a function of detector temperature and the accuracy of the measurement of elemental abundance line ratios as a function of detector temperature. Data from the student laboratory experimentation suggested that the detector temperature remain at or below -75°C to minimize intrinsic noise properties. Data from the computational analyses of the spectral resolution model suggest consistent results that the detector temperature remains at or below -55°C to remain within the established REXIS requirements.

The combination of these three results leads to the author's recommendation that a detector temperature requirement be set that the temperature of the CCD detector onboard REXIS shall not exceed -55°C and that a detector temperature goal be set that the temperature of the CCD detector shall not exceed -75°C.

Acknowledgments

For the completion of my undergraduate journey through MIT and this thesis I am grateful to my advisors and supervisor Dr. Sara Seager and Dr. Richard Binzel.

Dr. Seager has been an incredible advisor throughout the last two years. She is a source of inspiration and motivation, always challenging me to learn new things – professionally and personally – and to apply the information I already know. She has given me the confidence to continue the degree and even shared personal examples of innovation, insight and grit to help my studies.

Dr. Binzel has been an asteroid to rely on; I am grateful for his advice and patience, his direction regarding the work on the REXIS project and his capacity for an objective view of every problem – always providing guidance and believing in me.

I would like to acknowledge with gratitude the assistance and support of Niraj Inamdar, Matthew Adendorff, Jane Connor, the MIT/Harvard REXIS Team, members of the OSIRIS-REx mission, and members of the MIT Earth, Atmospheric & Planetary Science Department.

For the unconditional belief and support I received from Dr. Susan Mausshardt, Dr.'s Carolyn & Adam Conklin, Dean David Randall, Dr. Silk and Ms. Barbara Lechner I will forever be grateful.

I thank MIT, the Linda Gronlund Fund and Mr. & Mrs. Dan and Marian Martin for their financial support.

Biographical Sketch

The choices of my life have given me a unique set of opportunities and experiences but have brought me a most interesting set of challenges, all of which have affected the person I am and am capable of becoming.

In 2004 I was a busy, complicated and misaligned young girl who wrote a profound personal statement and was admitted to MIT. I will safely say that the unbridled optimism of youth combined with the allure of a degree from MIT is a dangerous combination. In 2005 I came to MIT after seventeen years of reinforcement of bad behaviors. The challenges that ensued were not just about trying to separate the past from the present but about severing whatever fictitious tie was keeping me anchored to a chaotic family environment, continually reminding me that no matter what I attempted I couldn't measure up – handicapped by a y-chromosome. Confronting the demands of the scholastic environment at MIT, I did the only thing I knew how to do at that point… I ran.

My childhood raised me with mechanical skills – machining, welding, auto mechanics – languages, martial arts and combative survival as well as a mental and emotional strength that can only be conditioned growing up with an ex-KGB agent as a father and a subservient mother. Despite our strained relationship, in part, my mission is a result of those two people who created me and built me: Mr. Sándor Alex Megyery and Mrs. Erzsébet Megyery.

In 2008 I left MIT to discover and erect my own definitions of peace, clarity, integrity and purpose. After several months of a kinesthetically-focused education, with everything from kayaking, surfing and mountaineering, I reevaluated my situation.

With the help of older, and what I am sure are wiser eyes, I established a set of goals that are both worthy and achievable in improving the future, not only for myself, but, also for the world we live in. In furtherance of that goal, I relocated and attended the University of Washington and targeted employment, to challenge and improve myself and to apply the discipline that I achieved to teach and train others. The planning and execution of the steps required to return to MIT would not have been possible without the support of dear friends Heidi Sitton and Alan Heddings.

In 2011 I returned to MIT with focus, equilibrium, anticipation and integrity. The two-year journey upon my return has become a locust of vectors all charged with the energy and destination of fulfillment. The alignment that ensued within myself has been rapid and extraordinary. My adventures since my return to MIT have continued to be varied, and those journeys have helped me to find center, purpose and home. Not long after my return, the MIT Earth Resources Laboratory took a team of students on a geophysics groundwater project to St Lucia and for the first time in my life I felt that I had come home.

The challenges of how I grew up have given me a deep connection to the people and culture of countries that are less technologically developed than the United States. My connection to St Lucia and the West Indies is profound and intimate. For the summer of 2012 I was awarded an MIT Public Service Center Project Fellowship Award as well as Undergraduate Research Opportunities Program funding to support my project in water security, public health and safety, working alongside the Caribbean Environmental Health Institute (CEHI) in St Lucia. For four months I lived and

worked on-island and found family in community through my coworkers at CEHI and a local cycling charity group called Project Breakaway. Every member of these teams was an inspiration, a friend, and a source of encouragement for my return to MIT to complete my studies and to return to St Lucia someday soon.

I would like to exclusively thank MIT Professor Frank Dale Morgan for taking a chance on me and supporting my ideas when most everything inside of him suggested otherwise. From my work with CEHI I would like to extend my appreciation to Dr. Chris Cox and Ms. Shermaine Clauzel. These two worked closely with me for the entirety of my project and believed in me even when I was battling Dengue Fever; they also saw first-hand just how St Lucian I had become. This wonderful family reminded me that we work to live rather than live to work and cautioned me to avoid the trap of spending fifteen years building a great career, only to throw it in one day upon realizing that I had juggled life and work to make everyone happy – but myself.

The Project Breakaway group rides with a purpose and taught me that having family makes your life richer; in that, family can be found anywhere, and because of them I shared a fulfilled life in St Lucia. I would like to thank all the members of Project Breakaway for reminding me that there is a different way to live and the pursuit of such happiness is the chase of a lifetime. I would herein like to include: Mr. Ernest Ottley and Mrs. Brenda Ottley, Mr. Ross Stevenson, Mr. Raymond Volney, Kurt and Kirk Miraj, Richard Monplaisir, Jason Tameh, Roderick Cherry; Andrew, Bev and Gillan Moses, Chandoy Moses, Fidel Mangal, Oliver Cadet, Mr. L. Ryan Joseph and additional members of Project Breakaway.

Upon my return to MIT from St Lucia it was time to complete my thesis work and not simply put a check in a box. I have been a part of the MIT REXIS Instrument team as a student scientist since September of 2011. This project has given me the perfect opportunity to combine my varied undergraduate studies that span earth sciences, space sciences, engineering, and physics into a concrete and valuable contribution.

I am grateful for the challenge I have been privileged to be a part of: the MIT undergraduate experience.

I have always told myself I can pass any test a human being can pass; I plan to prove it.

Dedication

Words cannot express the gratitude I have for the following individuals who have been and continue to be my best friends and my family.

I am grateful for the never-ending love and encouragement of my brother and best friend, my comrade, with whom I survived the war and torture of our childhood, Mr. Sándor (Alex) Megyery, and his incredibly supportive wife, Mrs. Alethea L. Megyery. My brother Alex is my rock and their combined force has reminded me that fulfillment will not be found in all the materials, school and high expectations others have put out there for you, but rather that contentment is found within one's self. They have helped me to figure out just what that means.

Parallel in direction and magnitude are the contributions of the couple that have filled the shoes in my soul and spirit as parents: Mr. Walt Giuffrida and Ms. Jacqueline Wheatley. Without Walt's attention and dedication to the old Suzy, that little girl so full of life, I would have never known of MIT at that young age. Upon my admission to MIT they gave me a personalized copy of Emily Post's *Etiquette*, a little black dress, and charged me to sever myself from my past and to go out into the world and become the sweetest person I can be.

A childhood without the feeling of family taught me to simplify and that your selection of friends indeed *are* your family. With that, I adore my brother Joel Ramine and sister Cypriana George in St Lucia, my best friends from my MIT experience Brandon Reese, Sebastian Figari, Dhaval Adjodah and Melina Flores, and the unparalleled support of David Ellis.

I want you to know that I am very, very fortunate. I have gone through many different experiences to come to this new journey. I fully believe with all my heart and soul that life finds me even more equipped to take this next leap. I believe I will glean so much more out of it because there's a more complete Suz. I know I have some amazing adventures ahead of me... some of these I could have missed if I were my younger self.

My wish for all who read this is that you are content with you. Many people spend their whole lives looking for that contentment only to have missed it inside themselves. The world is at your fingertips, it's all in how you see it, and I hope you see it – especially Ms. Ashlynn Jones.

I lovingly dedicate this thesis to Alex & Alethea Megyery, Walt Giuffrida & Jacqui Wheatley, Joel Ramine, Cypriana George, Brandon Reese, Sebastian Figari, Dhaval Adjodah, Melina Flores, and David Ellis.

Ms. Ashlynn Jones, I believe in you.

Table of Contents

List of Figures

List of Tables

Acronyms

ADU	-	Analog/Digital Unit
BSE	-	Bulk Silicate Earth
CCD	-	Charge-Coupled Device
CCID	-	Charge Coupled Imaging Device
CTE	-	Charge Transfer Efficiency
CXB	-	Cosmic X-ray Background
EAPS	-	Earth, Atmospheric & Planetary Sciences, [Department of]
GSFC	-	Goddard Space Flight Center
MIT	-	Massachusetts Institute of Technology
MOS	-	Metal Oxide Semiconductor
NASA	-	National Aeronautics and Space Administration
NEAR	-	Near Earth Asteroid Rendezvous
OBF	-	Optical Blocking Filter
OSIRIS-REx	-	Origins Spectral Interpretation Resource Identification Security Regolith Explorer
REXIS	-	REgolith X-ray Imaging Spectrometer
SNR	-	Signal-to-Noise Ratio
SSL	-	Space Systems Laboratory
SSP	-	Standard Sample Plate
SXM	-	Solar X-ray Monitor
TPM	-	Thermophysical Modeling
XGRS	-	X-ray/Gamma-Ray Spectrometer
XIS	-	X-ray Imaging Spectrometer
XRF	-	X-Ray Fluorescence
XRS	-	X-Ray Spectrometer

Chapter 1: Introduction

1.1. Project Scope

This thesis was written in partial fulfillment of the Bachelor of Science degree in the Department of Earth, Atmospheric & Planetary Science (EAPS) at the Massachusetts Institute of Technology (MIT). The content of the thesis falls under the topic of geochemical remote X-Ray Fluorescence (XRF) spectrometry in the context of REgolith X-ray Imaging Spectrometer (REXIS), a Charge-Coupled Device (CCD)-based coded aperture soft X-ray (0.3-7.5 keV) telescope for remote geochemical XRF spectrometry.

REXIS has been selected as an education and public outreach element of the OSIRIS-REx mission investigation after a competitive selection process. As a student collaboration experiment, REXIS will be incorporated into the OSIRIS-REx spacecraft on a non-impact basis and will remain clearly separable from the rest of the OSIRIS-REx investigation. Data analysis will be handled as a student project. The REXIS project is a collaboration between students and faculty at MIT and Harvard University. At MIT, faculty leadership is provided by Professor David Miller, Professor Richard Binzel, and Professor Sara Seager. At Harvard, the faculty leadership is provided by Professor Josh Grindlay. For other REXIS-related work that I conducted prior to this document, supplemental information is available in Appendix A of this thesis.

REXIS will fly onboard the Origins Spectral Interpretations Resource Identification Security Regolith Explorer (OSIRIS-REx) asteroid sample return mission that will be visiting the asteroid 1999 RQ36 and sending a sample back to Earth. The spacecraft will conduct mapping, which will allow comparison with Earth-based observation, and the mapping of surface organics, volatiles and potential resources. Finally, the mission will map surface features to show the correlation of soil pools with local gravity and asteroid rotation.

OSIRIS-REx will accomplish these through a variety of instruments on board, among them, REXIS. All aspects of the mission, including REXIS, lead to identifying the best sampling site on the asteroid. REXIS will map the surface elemental abundance ratios of 1999 RQ36 globally and spatially, contextualizing the physical sample return, using CCD-based, fluoresced X-ray detection.

In the general case, XRF is a well-established technique in the laboratory for performing both qualitative and quantitative elemental analysis of samples. CCD-based, fluoresced X-ray detection of a continuous source, with a variety of geochemical elements present, will produce a spectrum or histogram. The spectrum will span a range of characteristic elemental energies with specific intensities. To discriminate fluorescent X-rays of major elements, a specific energy resolution, here known as spectral resolution, is required. Spectral resolution is also dependent on an effective detection area to accumulate statistically significant counts of X-ray photons in a given integration time for quantitative elemental analysis. Spectral resolution degrades with detector temperature and detector degradation due to radiation damage. Quantifying the limits for accurate spectral resolution is vital to XRF science.

This thesis outlines laboratory experimentation that was conducted on the REXIS CCDs and analyzes derivative work that was completed from the results of that experimentation to define inputs into a spectral resolution model. The results of that spectral resolution model then dictate the photon count detection accuracy and the temperature required of the CCD to meet the REXIS requirements. It is mandatory to meet these requirements in the CCD detector for efficient spectral resolution and useful spatial resolution of the asteroid surface to complete the mission science goals.

1.2. Audience

I have written this thesis with the express purpose of accessing several different audiences, each of who may find interest in specific sections of the thesis, but not others. It is the intention that some of the results of this report be used to improve the scientific community's understanding of the limits of remote geochemical CCD-based XRF sensing as detector conditions degrade.

The groups that I anticipate being immediately interested in this thesis include the REXIS project partners, to include the MIT Space Systems Laboratory (SSL), the MIT EAPS Department, the MIT Kavli Institute for Astrophysics, the Harvard College Observatory, the Harvard Department of Astronomy, the NASA Goddard Space Flight Center (GSFC). It is my hope that this thesis contributes to the scientific and engineering development of the REXIS Instrument and future Instruments of this nature. Also, current and future MIT students from the MIT EAPS and Physics Departments who may express interest in learning more about XRF and the limits of the CCD-based detection technique for their own projects; this thesis can serve as an introduction for them.

1.3. REXIS Mission Objectives

The REXIS Instrument will fly onboard the OSIRIS-REx spacecraft as one of five Instruments. REXIS will provide an X-ray global map of 1999 RQ36, complementing core OSIRIS-REx mission science.

1.3.1. OSIRIS-REx Mission

NASA will launch the OSIRIS-REx spacecraft in 2016 to the primitive, near-Earth asteroid 1999 RQ36 (101955). The spacecraft will use a robotic arm to pluck samples from the asteroid and send them back to the Earth; this will be the first U.S. mission to carry samples from an asteroid back to Earth. OSIRIS-REx will approach the asteroid in 2019. The next six months of the mission will be spent conducting surface mapping with a variety of different instruments. The science team shall then choose the sample site and the spacecraft will move closer to take the sample. The sample will then be sent back to Earth for analysis.

1.3.1.1. OSIRIS-REx Project Motivation

Telescopic observations have helped define the orbit of asteroid 1999 RQ36 that brings it close to the Earth every six years. It is critical to know the orbit of 1999 RQ36 because recent calculations produced a 1 in 1800 chance of impact with Earth in the year 2182 (The University of Arizona, NASA Goddard Space Flight Center, 2013). Part of the OSIRIS-REx mission is to refine understanding of effects on this orbit and its intersection with Earth's.

The primary mission objective is to return the first pristine sample of carbon-rich material from the surface of a primitive asteroid. The target asteroid, near-Earth object 1999 RQ36, is an accessible, volatile- and organic-rich remnant from the early solar system (The University of Arizona, NASA Goddard Space Flight Center, 2013).

Carbonaceous asteroids, such as 1999 RQ36, are the direct remnants of the building blocks of terrestrial planets (Jagoutz, 2011). Their chemical and physical nature, distribution, formation, and evolution are fundamental to understanding planet formation and the origin of life. In contrast to stony and iron asteroids that formed within 2-3 AU of the Sun, the carbonaceous asteroids contain a large fraction of organics and are volatile rich. Although 1999 RQ36 is currently located at a close distance to the Sun, it originally formed beyond 2-3 AU and has recently, within the past few million years, been moved into its current orbit by the gravity of the major planets (The University of Arizona, NASA Goddard Space Flight Center, 2013; A. Milani, 2009).

1.3.1.2. Mission Science Objectives

Telescopic observations have revealed some basic properties of 1999 RQ36. They indicate that 1999 RQ36 is very dark and has been classified in a rare subgroup of the dark, carbonaceous asteroids that are considered "primitive" having undergone little processing from their time of formation (The University of Arizona, NASA Goddard Space Flight Center, 2013).

Through sample, mapping and measuring the asteroid, the science objectives define the questions the mission wants to ask about the asteroid and the information the mission hopes to learn.

From the Mission's Science Objectives webpage (The University of Arizona, NASA Goddard Space Flight Center, 2013), these Objectives are:

- Return and analyze a sample of pristine carbonaceous asteroid regolith in an amount sufficient to study the nature, history, and distribution of its constituent minerals and organic material.
- Map the global properties, chemistry, and mineralogy of a primitive carbonaceous asteroid to characterize its geologic and dynamic history and provide context for the returned samples.
- Document the texture, morphology, geochemistry, and spectral properties of the regolith at the sampling site in situ at scales down to millimeters.
- Measure the Yarkovsky effect, a thermal force on the object, on a potentially hazardous object and constrain the asteroid properties that contribute to this effect.
- Characterize the integrated global properties of a primitive carbonaceous asteroid to allow for direct comparison with ground-based telescopic data of the entire asteroid population.

1.3.2. The REXIS Instrument

Sample return is the principal objective of the OSIRIS-REx mission. Maximizing the science yield from the sample analysis requires the best possible asteroid context for the returned sample. The REXIS science objective is to complement onboard mineral mapping by adding spatially resolved elemental abundance ratio mapping achieved through X-ray spectrometry.

1.3.2.1. REXIS Instrument Overview

REXIS is a coded aperture soft X-ray (0.3-7.5 keV) telescope that images X-ray fluorescence line emission produced by the interaction of solar X-rays and the solar wind with the regolith of 1999 RQ36. Images are formed with 21-minute arcminute resolution (4.3 m spatial resolution at a distance of 700 m). Imaging is achieved by correlating the detected X-ray image with a 64 x 64 element random mask (1.536 mm pixels). REXIS will store each X-ray event in order to maximize the data storage usage and to minimize the risk. The pixels will be addressed in 64 x 64 bins and the 0.3-7.5 keV range will be covered by 5 broad bands and 11 narrow line bands. A 24-sec resolution time tag will be interleaved with the event data to account for 1999 RQ36 rotation. Images will be reconstructed on the ground after downlink of the event list. Images are formed simultaneously in 16 energy bands centered on the dominant lines of abundant surface elements from O-K (0.5 keV) to Fe-KB (7 keV) as well the representative continuum. During orbital phase 5B, a 21-day orbit 700 m from the surface of 1999 RQ36, a total of at least 133 events/asteroid pixel/energy band are expected under 2 keV; enough to obtain significant constraints on element abundances at scales larger than 10 m (The University of Arizona, NASA Goddard Space Flight Center, 2013).

1.3.2.2. REXIS Requirements

As it is the REXIS design goal to complement OSIRIS-REx Science Objectives, the REXIS Instrument Requirements are a direct flow-down from the following OSIRIS-REx Science Requirements (The University of Arizona, NASA Goddard Space Flight Center, 2013) that REXIS anticipates contribution to:

- Surface Chemistry Functional Requirement: OSIRIS-REx shall document the texture to sub-mm resolution, morphology, geochemistry, and spectral properties of the sampling site.
- Surface Chemistry Performance Requirement: OSIRIS-REx shall determine mineral, organic, and phase abundances that have spectral absorptions ≥5% on the surface of 1999 RQ36, at a global spatial resolution of 50 m or better.
- Volatile Outgassing Requirement: OSIRIS-REx shall search for and characterize regions of active volatile outgassing from the surface of 1999 RQ36.

In order to complement the OSIRIS-REx geochemical requirements, the following are the REXIS Instrument requirements:

REXIS has the following Level 1 requirements to (1) measure global elemental abundances with sufficient sensitivity to distinguish the mean global composition of the asteroid for classification and (2) perform an elemental abundance analysis of the surface of 1999 RQ36 with sufficient spatial resolution to contribute to sample site selection.

Table 1: REXIS Level 1 Requirements

ID#	Level 1 Requirement
REX-1.1.1	REXIS shall measure global elemental abundances of asteroid 1999 RQ36 with sufficient sensitivity to distinguish the mean global composition of the asteroid among major meteorite groups, including CI, CM, CV carbonaceous chondrites Rationale: Elemental abundance will complement the mineralogical abundance measurements made by the other spectrometers, helping to resolve ambiguities. The sensitivity should target elements that will help distinguish among meteorties that could originate from RQ36
REX-1.2.1	REXIS shall perform an elemental abundance analysis of the surface of asteroid 1999 RQ36 with ≤ 50m spatial resolution to contribute to sample site selection Rationale: Elemental abundance will complement the mineralogical abundance measurements made by the other spectrometers, helping to resolve ambiguities. With enough resolution, this information can be used to help select the sample site

(MIT/Harvard REXIS Team, 2013)

REXIS has the following Level 2 requirements describing (1) the accuracy requirement for measuring global ratios of elements of the major meteorite groups, (2) the abundances of key elements, O, Fe, and Mg, with a specific SNR and spatial resolution in order to aid in sample site selection, (3) the abundance of Si with a greater enhancement than those of (2) because all elemental ratios are in reference to Silicon, and (4) multiple element detection through spectroscopic identification with a specific SNR in order to understand the elemental composition of 1999 RQ36.

Table 2: REXIS Level 2 Requirements

ID#	Level 2 Requirement	Parent
REX-2.1.1	REXIS shall be able to measure the global ratios of elements: Mg/Si, Fe/Si, S/Si with an accuracy of 10% Rationale: Element ratio measurement aids in the classification of 1999 RQ36 into one of the major meteorite groups, and is less prone to systematic errors	REX-1.1.1
REX-2.2.1	REXIS shall measure the abundance of the following elements - Fe and Mg at a factor of > 2 at SNR >5 with a spatial resolution of 50m Rationale: These elements can inform the selection of the sample site and can be feasibly detected at this SNR and at this factor of enhancement	REX-1.2.1
REX-2.2.2	REXIS shall measure the abundance of Si at a factor of > 3 enhancement at SNR > 5 with a spatial resolution of 50m Rationale: Silicon can inform the selection of the sample site and can be feasibly detected at this SNR and at this factor of enhancement	REX-1.2.1
REX-2.3.1	REXIS shall measure the global abundances of the following elements - Fe, Si, Mg, S with a SNR of > 10 Rationale: Multiple element detection through spectroscopic identification is crucial to understanding the elemental composition of 1999 RQ36. SNR assumes 1999 RQ36 is a carbonaceous chondrite.	REX-2.1.1

(MIT/Harvard REXIS Team, 2013)

Meeting Level 2 requirement REX-2.1.1 is a goal of this thesis. A thorough explanation of the model developed to meet Level 2 Requirement REX-2.1.1 will be discussed in Section 3.2 of this thesis.

REXIS has the following Level 3 requirements describing spectral resolution requirements to discriminate unique XRF lines from each other and the Field of View (FOV) requirement in order to collect a quantity of photons statistically large enough to resolve higher energy lines.

Table 3: REXIS Level 3 Requirements

ID#	Level 3 Requirement	Parent
REX-3.1.1	REXIS shall have a spectral resolution (FWHM) as follows: <80 eV at 0.5 keV <100 eV at 1 keV <120 eV at 2 keV <150 eV at 4 keV <200 eV at 6 keV Rationale: Allows for the distinction of XRF lines from each other. (Assumes < -50 degree C operating temperature)	REX-2.2.1 REX-2.2.2 REX-2.3.1
REX-3.2.1	REXIS shall have a circular field of view (FOV) (FWZI) of 48 degrees Rationale: The FOV must be large to collect enough photons to resolve high energy lines; however, the influence of cosmic X-ray background must also be limited. The REXIS FOV includes the entire visible surface of the asteroid at an orbit larger than 750m (550m from the nearest surface). The expected Cosmic X-ray Background (CXB) is less than 11 cps at the orbit less than 1200m, which is acceptable under the 1.5 GB data limit (i.e. >200cps expected from RQ36). At the expected 1000m orbit radius in Phase 5B, the FOV also allows ±3 degs offset with the asteroid in more than 20% of the coding fraction.	REX-2.2.1 REX-2.2.2 REX-2.3.1

(MIT/Harvard REXIS Team, 2013)

Meeting Level 3 requirement REX-3.1.1 is also the subject matter of this thesis. A thorough explanation of the model developed to meet Level 3 Requirement REX-3.1.1 will be discussed in Section 3.2 of this thesis.

In order to meet these requirements, and hopefully REXIS aims, discussed in Section 1.3.2.4, the REXIS instrument preliminary design is introduced in the next section.

1.3.2.3. REXIS Design Components

To fulfill the above REXIS Science and design requirements, the REXIS instrument has the following preliminary design:

Figure 1 depicts the key components of the REXIS preliminary design. Relative to this thesis is the coded aperture mask and the detector plane.

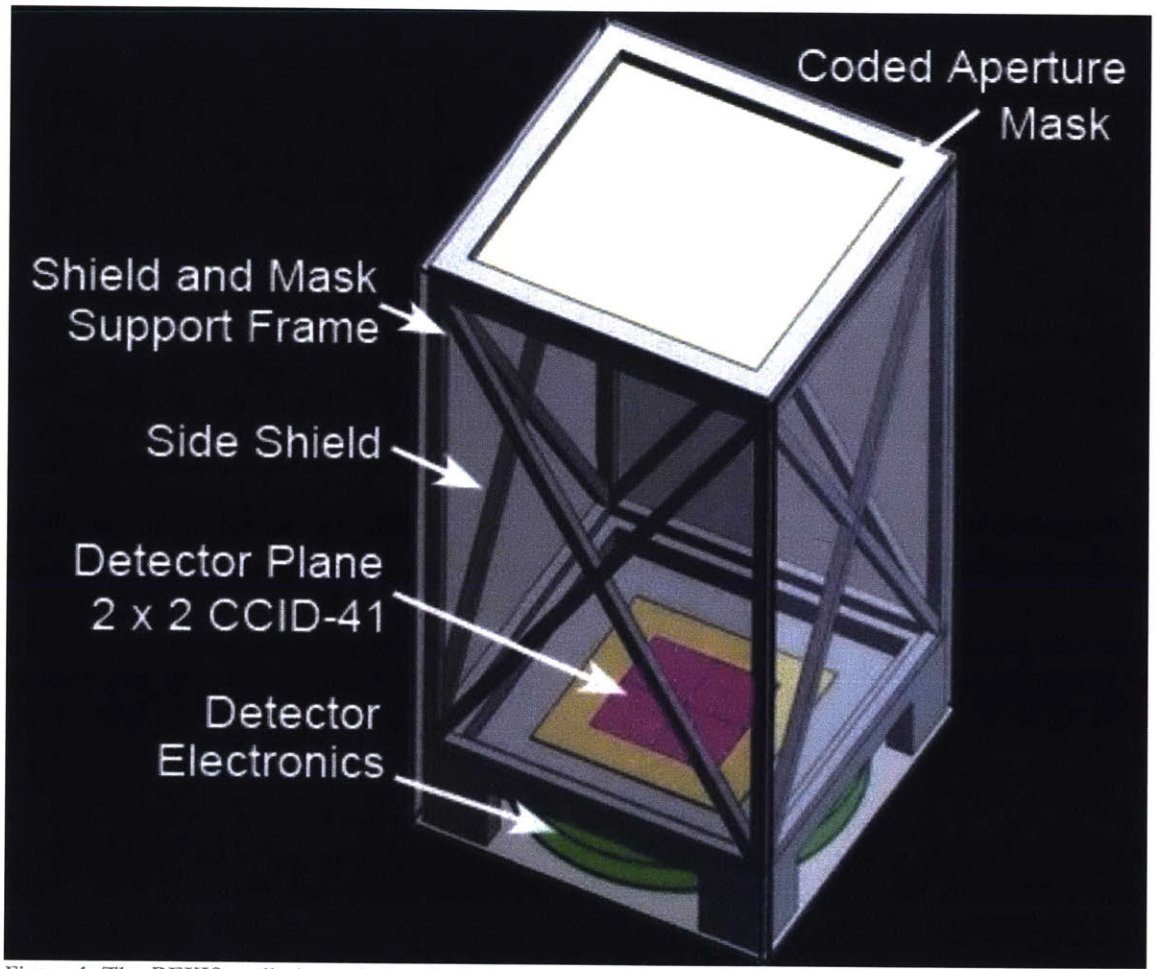

Figure 1: The REXIS preliminary design depicting key components to contextualize the CCDs to be used in the REXIS instrument (Image Credit: MIT/Harvard REXIS Structures Team, 2011).

Coded aperture imaging is typical for point sources and continuous sources, and so, the coded aperture mask will consist of a mask sufficient to perform the best possible deconvolution and correlation methods for image reconstruction with minimal noise as REXIS observes a continuous source, 1999 RQ36.

The REXIS detector plane will feature a 2 x 2 grid of CCID-41 CCD detectors that will be built by MIT Lincoln Laboratories. Optimizing the spectral resolution for these CCDs, defining the spectral resolution limits and the CCD requirements to meet these requirements is the focus of this thesis.

The REXIS design, including the CCID-41, is built on flight heritage to minimize associated risk factors. The Japanese Hayabusa spacecraft, formerly known as MUSES-C (launched 2003) was the first time a CCD had been used for the purpose of XRF spectroscopy on a planetary mission (T. Okada M. K., 2000). The Japanese Suzaku spacecraft (launched 2005) was Japan's 5th X-ray astronomy satellite; it is an Earth-orbiting observatory imaging various X-ray sources. Suzaku is equipped with four independent CCD-based X-ray Imaging Spectrometer (XIS) sensors that were built by MIT Lincoln Laboratory (K. Koyama, 2006). A thorough discussion on the flight heritage of REXIS can be found in Appendix B.1.

1.3.2.4. REXIS Science Aims

As a student collaboration experiment, REXIS will be incorporated into the OSIRIS-REx spacecraft on a non-impact basis and will remain clearly separable from the rest of the OSIRIS-REx investigation. Data analysis will be handled as a student project.

It is the hope of the REXIS team that the Instrument will successfully achieve its science objective to map the surface elemental abundance ratios of 1999 RQ36 globally and spatially. Achieving this objective, REXIS may be able to assist in contextualizing the physical sample return from the OSIRIS-REx spacecraft. Further, it is possible that with good conditions, successful completion of our objectives, and real-time data analysis is conducted, that REXIS science shall contribute to the sample site selection of the OSIRIS-REx Science Team.

1.4. REXIS Technological Baseline and Introduction

Meeting the REXIS Level 2 requirement REX-2.1.1, the accuracy requirement for measuring global ratios of elements, and Level 3 requirement REX-3.1.1, describing spectral resolution requirements to discriminate unique XRF lines from each other, is the subject matter of this thesis. A thorough explanation of the model developed to meet these requirements will be discussed in Section 3.2 of this thesis.

An X-ray detector such as the Lincoln-Laboratory CCID-41, which will be used in the REXIS Instrument, is grown from a single silicon crystal. Silicon is used because of the material's favorable charge transfer properties. The detector operates by collecting charge imparted by incoming photons on pixels etched into the crystal surface. The pixels hold the charge until the detector's electronics measure the charge at each pixel and then ground of 'refresh' the pixel array to begin the next imaging cycle.

The quality of X-ray spectrometry is dependent on (1) the efficiency of charge transfer and (2) the accuracy of charge measurement. High-energy particles from the Sun and deep space degrade the detector's ability to efficiently transfer charge, thereby reducing spectral resolution. These properties affecting the CCD's spectral resolution are all intrinsic to the detector. Specifically, the SNR of the CCD detector has a carry-over effect on the spatial resolution that can be attained.

The correct interpretation of X-ray measurements from the surface of 1999 RQ36 will require a detailed understanding of XRF science and the limitations of a CCD-based X-ray detector. CCD-

based X-ray detection produces a histogram of photon intensities, each with a characteristic energy and wavelength. Ideally, without intrinsic noise interference, the read-out from the detector would be a set of very sharp peaks for each line as delta functions. The widening of spectral lines can depend on a number of factors to include effects from the detector hardware, say, due to detector temperature.

To effectively discuss these factors that contribute to the degradation of a CCD's spectral resolution, Chapter 2 discusses the baseline by which these scientific processes occur and the detailed technology of these operations in order to accurately frame the scientific questions that this thesis proposes to answer. Chapter 3 introduces the investigations that have been conducted in order to test and model the limits that will 'break' or surpass the REXIS Instrument requirements REX-2.1.1 and REX-3.1.1. Finally, Chapter 3 clearly defines the scientific results of this analysis of the MIT/Harvard REXIS Team's work in the hope of expanding the REXIS Level 2 and Level 3 requirements by recommending additional instrument requirements to acquire useful scientific results from the instrument.

Chapter 2: Scientific Baseline & Physical Foundations of Operations

Meeting the REXIS Level 2 requirement REX-2.1.1, the accuracy requirement for measuring global ratios of elements, and Level 3 requirement REX-3.1.1, describing spectral resolution requirements to discriminate unique XRF lines from each other, is the driver of this thesis analysis. Chapter 2 discusses XRF science technology as it is relevant to REXIS at 1999 RQ36 (Section 2.1), the solar X-ray environment as it is relevant to the detection of elements by REXIS at 1999 RQ36 (Section 2.2), CCD-based coded aperture imaging (Section 2.3), and CCD-based XRF detection as it applies to the REXIS instrument at 1999 RQ36 (Section 2.4) to outline the background necessary to understand the science questions this thesis hopes to address.

2.1. Physical Foundations of Operation: XRF for Geochemical Remote Sensing

X-ray fluorescence (XRF) is a well-established technique in the laboratory for performing both qualitative and quantitative elemental analysis of samples. X-ray spectroscopy from an orbiting spacecraft can be used to identify elemental composition at the surface of an airless body such as 1999 RQ36. The crux of geochemical analyses of planetary bodies in the solar system is that only ratios, and not necessarily absolute concentrations, are similar between the different reservoirs. In the case of REXIS, these ratios are normalized to Silicon. The sun is the origin of the X-ray photons that fluoresce from the asteroid surface; however, the Sun is a continuous and time-variable source of X-rays. Solar X-ray emissions across all parts of the spectrum vary temporally, in terms of origin on the solar surface and in terms of the direction they are emitted. The effects of the solar X-ray environment are discussed in Section 2.2.

2.1.1. Introduction to X-ray Fluorescence

X-ray fluorescence (XRF) is a well-established laboratory technique for performing elemental analysis of samples both qualitatively and quantitatively. Usually an X-ray source is used to eject inner-shell electrons from the atoms in the sample by way of photoelectric absorption. The subsequent rearrangement of the atomic electrons gives rise to the emission of monoenergetic X-rays – the fluorescent X-rays – whose energies, in the 0.1-to 100-keV range, are characteristic of the specific chemical elements in the sample. Spectral analysis of these fluorescent X-rays can therefore provide us with information concerning the elemental composition of the sample.

As was proven during the Apollo 15 and 16 missions, major elemental composition can be determined through the remote XRF method for atmosphere-free planetary surfaces (T. Okada T. A., 2005; I. J. Adler, 1977). Solar X-rays irradiate a regolith surface to excite each atom of the uppermost surface materials. Immediately, those atoms settle to the ground state and X-rays characteristic of major elements are illuminated off the surface. However, intensity and spectral profiles of solar X-rays vary through time, which affects those XRF rays off the surface as well. The variability of the solar X-ray environment is discussed in Section 2.2. Therefore, major elemental composition can be mapped from the orbiting altitude with remote XRF spectrometry, together with concurrent monitoring of solar X-rays (T. Okada T. A., 2005). XRF telescopes have mission flight heritage that is included in Appendix B.1.

2.1.2. X-ray Fluorescence for Geochemical Remote Sensing

X-ray spectroscopy from an orbiting spacecraft can be used to identify elemental composition at the surface of an airless body in the following manner:

- X-rays from the Sun shining on an asteroid will produce significant X-ray fluorescence from the elements contained in the very surface of the asteroid (the top 1 mm)
- When an element fluoresces, it emits X-rays with discrete energies that are unique or characteristic of that element (the strongest being K α X-rays)
- The asteroid pointing portion of the X-ray spectrometer detects these characteristic X-rays of a particular energy range
- From an analysis of the measured energy spectrum, elemental composition can be inferred

The intensity of detected X-rays is a strong function of solar illumination and activity. This relation is quantified in Section 3.1. To ensure proper quantitative analysis, X-ray spectrometers point an additional X-ray detector sunward to directly measure the incident solar flux (Clark, 1979). The signal strength measured by the X-ray spectrometer will, in general, improve as the Sun approaches solar maximum and will be particularly strong during the random solar flares that produce brief periods of high-level, high-energy solar X-rays (N. Crosby, 1993).

By observing asteroids, we hope to gain an understanding of early solar-system history. Evidence that asteroids preserve information that cannot be acquired from the study of major planets and satellites alone comes from the study of meteorites. Examining meteorites has indicated their parent bodies to have a variety of thermal histories. Some have been untouched since their original accretion from the solar nebula, whereas others are the products of global melting and differentiation (R. Michelson, 2006). Asteroids are the best parent-body candidates for meteorites (Lim, 2005).

The derivation of surface chemistry from spectral observations requires assumptions about the physical nature of the surface and thus remains at least somewhat speculative. High energy solar X-rays directly induce the production of X-ray lines, the energies of which are characteristic for chemical elements present on the surfaces of rocky bodies. This emission is strongly dependent on the chemical composition of the surface as well as on the solar spectrum (I. Adler J. T., 1970; I. Adler J. G., 1972; P. Clark I. A., 1978; Clark, 1979; L. Yin, 1993). Generally, the strength of the given line indicates how much of a given component, a major element, is present. Soft X-rays are readily attenuated, so the atmosphere must be virtually non-existent for X-rays to be produced and detectable from orbit. Also, an X-ray source must be in close enough proximity to generate lines which have sufficient SNR to be measurable by a remote detector during its encounter with a body. This limitation restricts XRF experiments to the sunlit surfaces of atmosphereless bodies in the inner (<3 AU) solar system, when the Sun is used as the primary source (I. Adler J. T., 1970; I. Adler J. G., 1972).

When solar X-rays interact with atoms at the very surface (to a depth of tens of microns), characteristic X-ray K α fluorescent lines for the major elements in this very surficial layer are produced. The solar flux, which is much more intense at lower energies, is sufficient to generate measureable lines not only for the major elements with lower energy lines such as Mg, Al, Si, but even for the higher energy lines of Ca, Ti, and Fe, although longer integration times are required.

Providing the surface is sufficiently "gardened" or mixed by micrometeorite impact over long periods of time, as was generally the case on the Moon, measurements made of the surficial layer are representative of underlying regolith (Taylor, 1975; P. Clark B. R., 1990). This may not be the case on asteroids, for example, and that result will have major implications for asteroid formation (P. Clark J. T., 1997).

2.1.3. Geochemical Remote Sensing of Asteroids

In geochemical analyses of planetary bodies in the solar system, only ratios, and not necessarily absolute concentrations, are similar between the different reservoirs. Nearly all of the carbonaceous chondrite meteorite groups are composed mainly of silicates, oxides and sulfides. The nature of geochemical remote sensing and the assumed composition of 1999 RQ36, that it is a carbonaceous chondrite, is the reasoning for this abundance-ratio approach to elemental mapping (MIT/Harvard REXIS Team, 2011).

It is believed that carbonaceous asteroids are representative of the early solar system and thus the building blocks of planets and the origins of life. A major research subject in Earth science is to understand planetary formation and differentiation processes. It is widely believed that the Earth formed in an area of the solar nebula that was depleted of the more volatile elements. Additionally, during or after accretion, the core formed due to the segregation of a Fe-rich liquid towards the center of the Earth (Jagoutz, 2011).

In geochemical sciences it is convention to separate the solar system, the Earth and any other planetary objects we have samples from, in different geochemical reservoirs. For example, some important reservoirs on the Earth are physical and geological entities like the core, mantle, crust and atmosphere. In more detailed investigations, the mantle itself is often separated into a multitude of smaller reservoirs or components, which do not necessarily differ in their physical or mineralogical properties.

Even using volcanic eruptions and mantle processes we can directly investigate only the upper ~150-200 km of the Earth. That is not much given the mean radius of the Earth (6,371 km). In order to make inferences about inaccessible reservoirs we make two major assumptions:

(1) We assume that the mantle is not compositionally layered. This assumption is justified if the mantle gets continuously stirred up and mixed by processes e.g., related to plate tectonics. Numerical simulations of mantle convection support this assumption. If that's true, then the uppermost 150-200 km of the mantle should be representative of the remaining ~3,283 km which we cannot access (Jagoutz, 2011). So, we can now claim that by direct sampling and chemical analyses of rock samples we can constrain the geochemistry of the entire silicate part of the Earth, called the Bulk Silicate Earth (BSE), which extends from the Earth's surface to the core-mantle boundary at 3,483 km. However, there are no samples available to constrain the composition of the core.
(2) We assume the compositions of certain asteroids, carbonaceous chondrites, are representative of the composition of the solar nebula (with the exception of H and He, which make up the bulk of the solar nebula). This assumption is justified because we can approximate the bulk composition of the Sun, which makes up ~99.85% of the mass of our

solar system. The composition of the Sun is indeed very similar to the relative abundance of elements in these asteroids, if internally renormalized. Since these asteroids fell on Earth, we have direct samples that approximate the bulk composition of our inner solar system (with the exception of the extremely volatile elements H, He) (Jagoutz, 2011).

The crux of geochemical analyses of planetary bodies in the solar system is that only ratios, and not necessarily absolute concentrations, are similar between the different reservoirs. In the case of REXIS, these ratios are normalized to Silicon. Nearly all of the carbonaceous chondrite groups are composed mainly of silicates, oxides and sulfides (Lim, 2005). The nature of geochemical remote sensing and the assumed composition of 1999 RQ36, that it is a carbonaceous chondrites, is the reasoning for this abundance-ratio approach to elemental mapping.

2.1.4. Thermal Effects on 1999 RQ36 – Mission Validation

The near-Earth object (NEO) (101955) 1999 RQ36 is a potentially hazardous asteroid known to have a non-negligible probability ($\sim 10^{-3}$) of impacting the Earth in the second half of the 22nd century (A. Milani, 2009). The interest in RQ36 boosted several campaigns of physical characterization: Radar delay-Doppler data allowed an accurate reconstruction of the shape of the object (H. Campins A. M., 2010) and showed that RQ36 is nearly spheroidal, has a diameter of ~0.5km and a double top-shaped silhouette. Thermophysical modeling (TPM) (A. W. Harris, 2002) of thermal infrared observations obtained from *Spitzer* indicates a size of 0.61km and a surface thermal inertia of ~600 J m^{-2} $s^{-0.5}$ K^{-1} (H. Campins A. M., 2010). Given an absolute magnitude of 20.9 (MPC) and a diameter of 0.5km, the geometric visible albedo is 0.03. This makes RQ36 a very dark object, consistent with a primitive organic-rich composition. Moreover, a recent study has identified the family of the low-albedo asteroid (142) Polana as the most likely main belt origin of RQ36 (H. Campins K. H.-A.-D., 2010).

Important issues related to sample return missions to primitive asteroids are (1) to determine the likelihood that the target candidate originates from a source region of primitive material in the solar system (e.g., the Polana family in the case of RQ36); and (2) to assess whether the surface (and the subsurface) of the object has been preserved from weathering processes active in space.

The implantation of ions by the solar wind and the bombardment of micrometeorites can alter the spectroscopic properties of asteroids (Hapke, 2001; S. Sasaki, 2001). However, these processes affect only the first few microns of the surface, while current sampling devices aim at collecting material at depth larger than a few millimeters.

Solar heating can also alter the original composition of NEOs – they can typically reach temperatures >370K, and the heat penetration depth is of the order of some centimeters for a body with a rotation period of some hours (J. R. Spencer, 1989; Harris, 1998).

There is a probability $\lesssim$20% that the surface temperature of RQ36 was ever above 600K (M. Mueller, 2011). However, for temperatures below 600K, the probability rises rapidly: there is a 50% and 80% probability that the temperature was $\gtrsim$500K and $\gtrsim$450K, respectively. The probability is ~1 that the surface was heated above 400K (M. Mueller, 2011).

We expect at least part of the material of RQ36 to be of similar composition as carbonaceous meteorites, as suggested by their similarity in spectral properties (M. Mueller, 2011). In these meteorites, around 25% of the organics are present as solvent-soluble or free organic matter, but the majority is in the form of a complex solvent-insoluble macromolecular material (Sephton, 2002).

In order to measure the kinetic parameters for thermal degradation of organic matter in the carbonaceous meteorite Murchinson, Delbo et al. (M. Delbo, 2011) have performed laboratory-heating experiments. They found that at 370K the aliphatic C-H bond of the insoluble organics is lost approximately within 200years. However, the bulk organics of Murchinson are lost in only on year at 370K (or 200 years at 300K). Lauretta et al. (D. S. Lauretta, 2001) have also studied the release of volatile elements as a function of temperature in CM and CV carbonaceous chondrites. Their results show that volatiles (in particular Hg) are released from most of the meteorites from about 470K.

From M. Delbo, (2011) it is noted that the surface of RQ36 is certainly dehydrated and its organic matter degraded. Some volatiles are also likely lost. Delbo and Michel (2011) concluded that if interlayer H_2O was present in the minerals at the surface of RQ36, this water is gone as the body entered the near-Earth space and surface temperature rose above the dehydration threshold. On the other hand, it is unlikely that water was lost from the dehydroxylation of phyllosilicates at the surface of RQ36, and it is even less likely that this happened at the subsurface, which is positive result for the objectives of a sample return mission (M. Delbo, 2011).

2.2. Physical Foundations: The Solar X-ray Environment

The solar output varies by three or more orders of magnitude across the energy range of interest and can be highly variable on timescales as short as minutes; thus, establishing the relationship between solar output, X-ray fluorescence line intensities, and surface concentrations is essential for quantitative results. Absolute elemental concentrations can be derived from instrumental measurements only when the quantitative nature of this relationship has been established.

2.3.1. The Solar X-ray Spectrum as a Function of Solar Activity

When REXIS will be operating, primarily phase 5B of the OSIRIS-REx mission, solar minimum is the expected solar state. The solar output is highly variable in the soft X-ray region and the rate of decrease of the incident flux is steeper than that of a higher solar states. Thus, sufficient solar flux to induce the fluorescent X-rays required to effectively detect Mg/Si and S/Si ratios is expected for the quiescent conditions that are expected during REXIS encounter with 1999 RQ36.

The solar spectrum consists of a continuum, which is generated by thermal bremsstrahlung and Radiative recombination, with superimposed major lines that result from emission due to transitions in H- and He-like ions (P. Clark J. T., 1997). The sources for these lines are ions with appreciable abundances in active regions. In modeling the solar output in their region of interest (1 to 10 KeV), Clark and Trombka (P. Clark J. T., 1997) used the best-published levels of solar output (Zombeck, 1990) over a range of levels of solar output, with only major lines included in the spectra.

Solar output is highly variable in the soft X-ray region, both in overall intensity and slope (R. Kreplin, 1977; Donnelly, 1976; National Geophysical Data Center, 1991).

Table 4 outlines the main solar flare states by classification and gives approximate energy level ranges for each. REXIS will encounter 1999 RQ36 during a minimum or 'quiet' solar state. A graphical representation of these states can be seen in Figure 2.

Table 4: Classification of Solar Soft X-ray Output

Spectra	Solar Level	NEAR Proportional Counters $0.5 - 10\ keV$ $(erg\ cm^{-2}s^{-1})$	GOES $1 - 8A$ (Wm^{-2})
Minimum		1.7×10^{-5}	0.1×10^{-8}
Quiet	A1	5.0×10^{-5}	1.0×10^{-8}
Mid-Cycle	A5	8.8×10^{-5}	5.0×10^{-8}
Subflare	B1	4.0×10^{-4}	1.0×10^{-7}
Low flare	C1	1.4×10^{-3}	1.0×10^{-6}
High Flare	M1	1.7×10^{-2}	1.0×10^{-5}

(P. Clark J. T., 1997)

Some of the various solar states, described in Table 4 above, are graphically depicted in Figure 2 below.

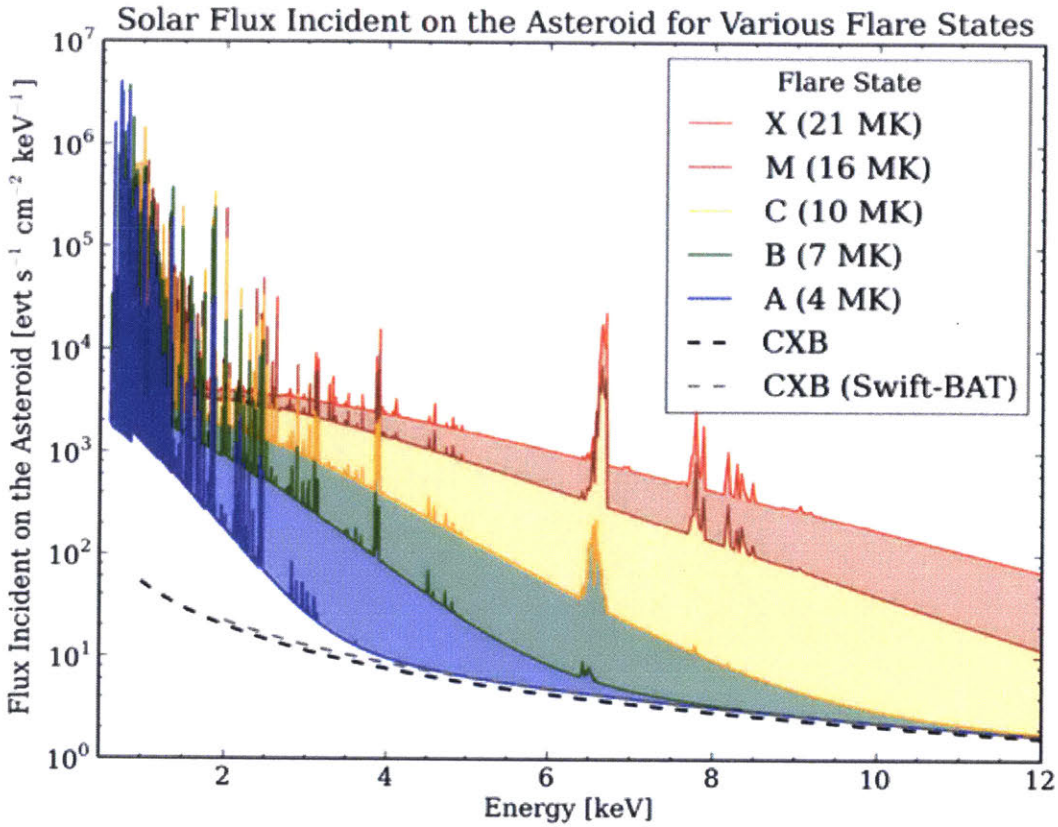

Figure 2: Graphical depiction of the solar flux for various flare states ranging from very low flux (Class A, ~4 MK) to very high flux (Class X, ~21 MK). Solar X-ray emissions across all parts of the spectrum vary temporally, in terms of origin on the solar surface and in terms of direction emitted. As can be seen in the graphic above, the lower the solar state, say state A compared to state B, state C and so on, the greater the rate of decrease of incident solar flux on the asteroid (Image Credit: Allen, 2012).

REXIS will encounter 1999 RQ36 during a minimum solar state; the solar flux for this quiet solar state is graphically depicted in Figure 3 below.

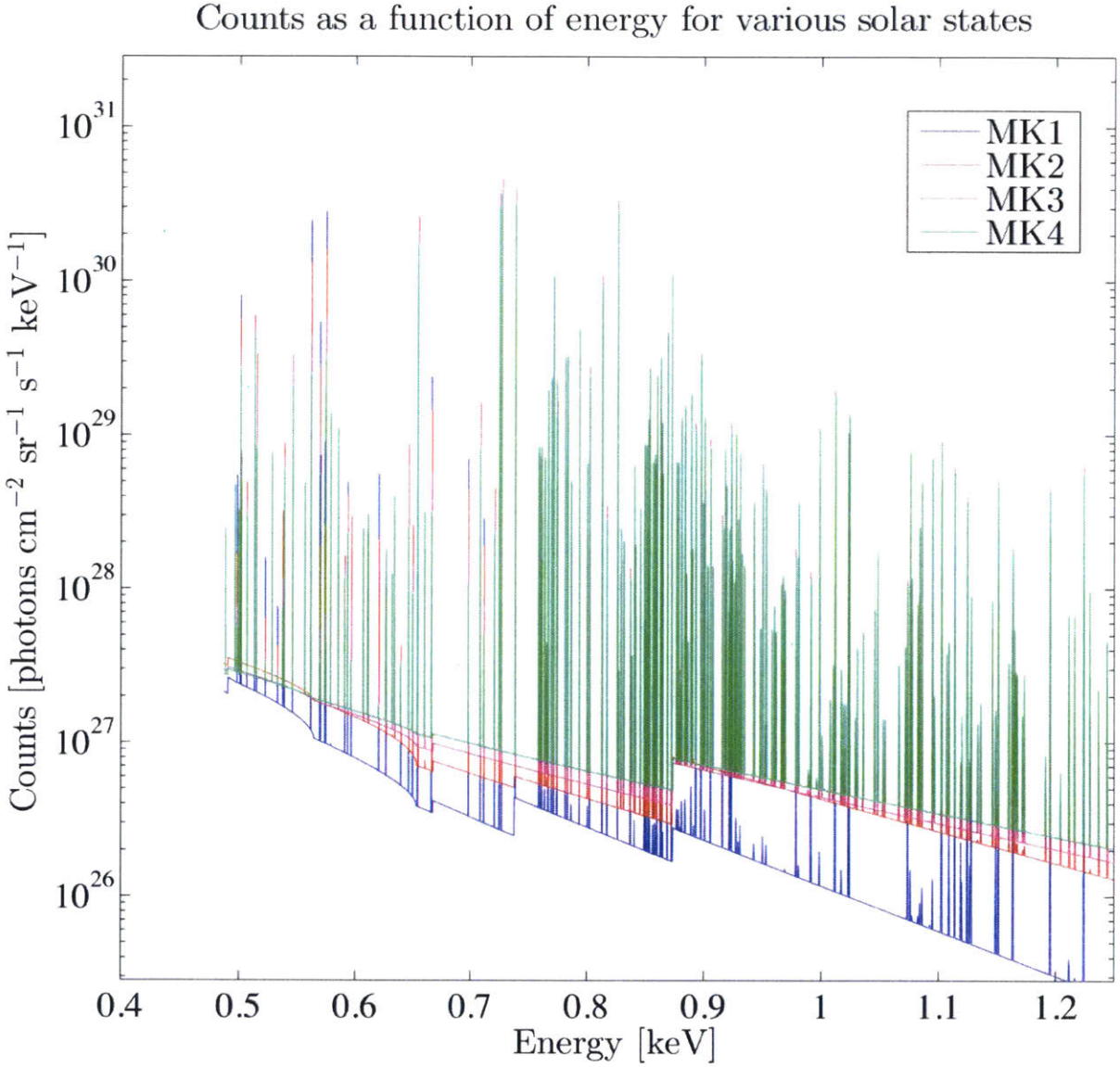

Figure 3: Solar spectrum X-ray counts as a function of the quiet or minimum solar states in Mega Kelvin emissions temperatures from the solar corona. This figure shows that at all quiet solar states, including minimum (MK 1), X-ray emissions vary continuously over time. Specifically, the solar intensity decreases by three to four orders of magnitude from 1 to 10 keV, the result being that fluorescent lines, as well as the scatter-induced background, have greater intensity at lower energies. Finally, the rate of decrease of incident solar flux on the asteroid is greater for the minimum solar state (MK1) than that of MK2 through MK4 (Image Credit: Lucy Lim, 2012).

The solar intensity decreases by three to four orders of magnitude from 1→10 KeV, the result being that fluorescent lines, as well as the scatter-induced background, have greater intensity at lower energies. As the level of solar activity increases, relatively more output occurs at higher energies, the slope of the spectrum becomes less steep, and the overall magnitude of the X-ray flux increases.

Coronal emission arises from highly ionized elements, at temperatures ~> 1MK (1 Mega Kelvin = 1,000,000 Kelvin). The physical understanding of this high temperature in the solar corona is still a fundamental problem in astrophysics, because it seems to violate the second thermodynamic law,

given the much cooler photospheric boundary, which has an average temperature of $T = 5785$ K (and drops to $T \sim 4500$ K in sunspots). However, it is important to interpret this emission spectrum of the solar corona because of the optically thin emission from the corona in soft X-rays (Aschwanden, 2006).

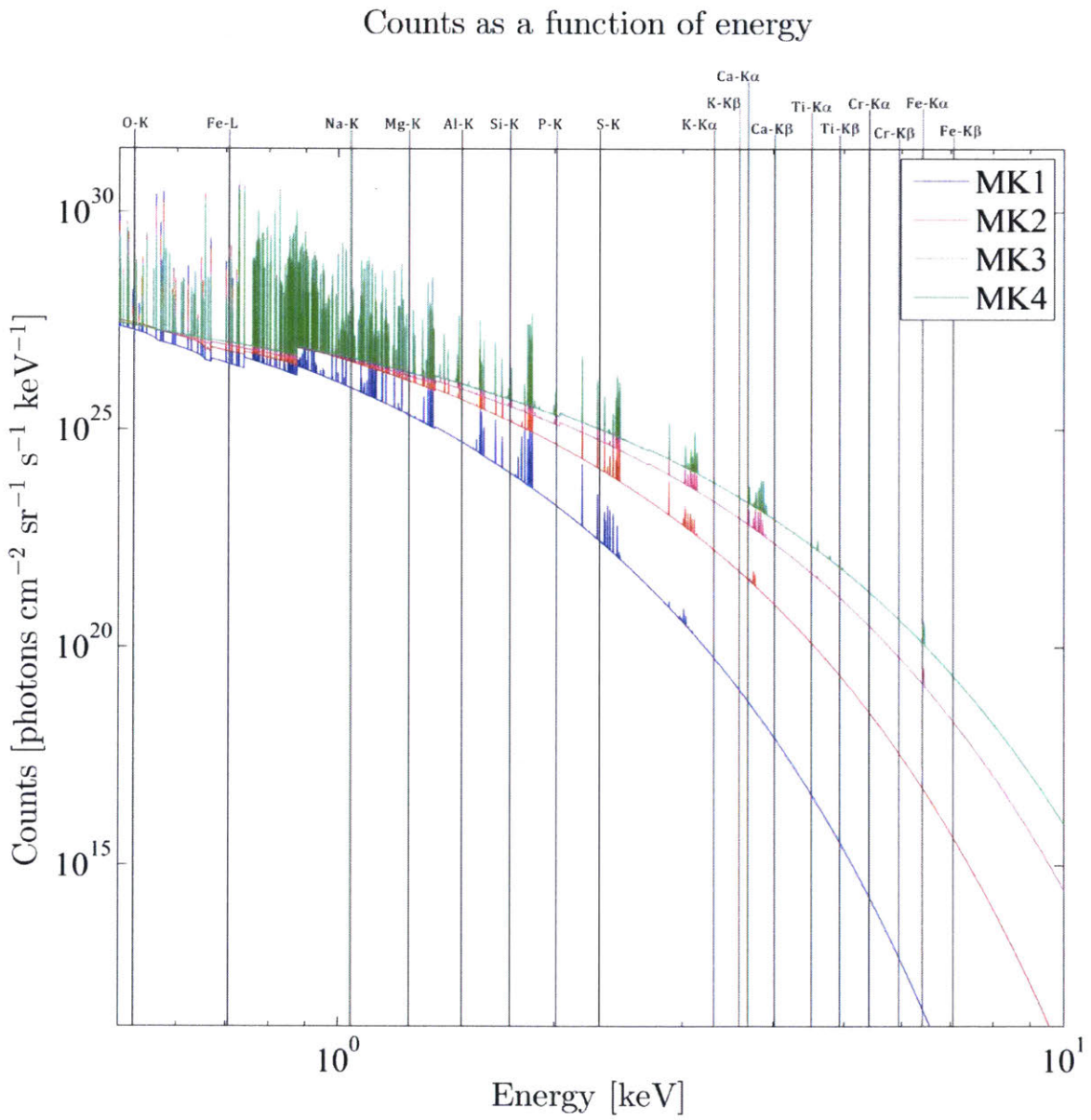

Figure 4: Solar spectrum X-ray counts as a function of various quiet solar states in Mega Kelvin emissions from the solar corona with the elemental X-ray emission lines of interest to REXIS marked vertically across the spectrum. This graphic clearly shows that the lower energy X-ray emission lines have greater intensity than those of higher energy lines, and the relative intensities of two adjacent lines is greater during a time of solar minimum than a state of greater solar activity (Image Source Credit: Lucy Lim, 2012; Image Source Edited: Megyery, 2013).

The process by which solar intensity decreases by orders of magnitude from 1→10 KeV, and that fluorescent lines, as well as the scatter-induced background, have greater intensity at lower energies, is called hardening. As the level of solar activity increases, relatively more output occurs at higher energies, the slope of the spectrum becomes less steep, and the overall magnitude of the X-ray flux increases. In Figure 4 we can see that elements with higher atomic numbers (Ca, Ti, and Fe) require a more active Sun to induce characteristic X-ray lines at intensities which are comparable to intensities for lower atomic number elements (Mg, Si, S) induced under more quiescent conditions. In general, for every order of magnitude increase in the level of solar activity, there is a corresponding order of magnitude decrease in the probability that the Sun will achieve that level of activity (P. Clark J. T., 1997).

When REXIS will be operating, primarily phase 5B of the OSIRIS-REx mission, solar minimum is the expected solar state. Thus, sufficient solar flux to induce the fluorescent X-rays required to effectively detect Mg/Si and S/Si ratios is expected.

2.3.2. Temporal Variations in Solar Activity

To expand on the data presented in Section 2.3.1, the Sun's output must be monitored and measured simultaneously with surface measurements due to the quick variability of incident solar flux and occurrence of solar flares. Figure 5 depicts this variation over four days in July 1990, validating the need for a Solar X-ray Monitor (SXM) to be coupled with the REXIS instrument aboard OSIRIS-REx.

More recent studies of the Sun's soft X-ray output have indicated that the Sun's output is highly variable on all timescales (Bouwer, 1983; R. Donnelly, 1981; N. Crosby, 1993). During the months around solar minimum (current OSIRIS-REx mission plan to encounter RQ36 is during solar minimum), less than one flare per day is reported on average; however, such flares, which can increase the intensity of the solar flux by 3 to 4 orders of magnitude, generally occur in clusters, with as many as 5 to 10 a day for as long as a few days. In between these periods of enhanced activity, weeks may go by when little or no flare activity occurs (Bouwer, 1983; R. Donnelly, 1981; N. Crosby, 1993).

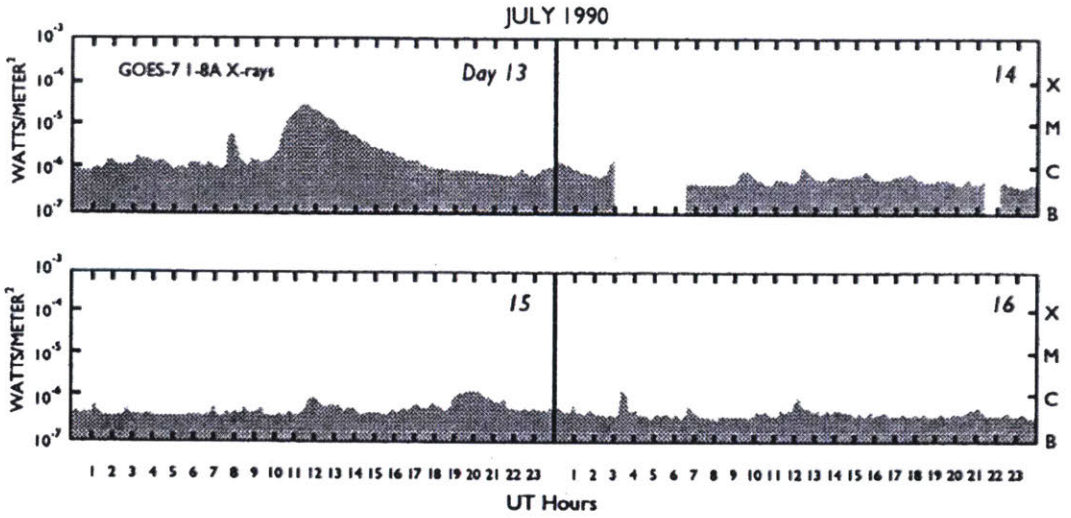

Figure 5: This figure shows minute to minute average solar flux over four days in July 1990. Features to note are the M-class flare and extended rise and fall time typical of large flares on July 13, and repeated occurrences of low level, C-class, flares on the remaining three days, while the more linear background is at a more quiescent subflare B-level (Image Credit: National Geophysical Data Center, 1991; Image analysis credit: P. Clark J. T., 1997).

Figure 5 (National Geophysical Data Center, 1991) illustrates the high variability possible in solar flux, even close to solar maximum as well as the apparent grouping of flare events. On July 13, measureable output is continuously at low-class flare level, and a class-M flare occurs, elevating the flux level for many hours. On the next 3 days, the measureable output is still above the typical Class B subflare level, with less than an order of magnitude variation to the level of a modest flare (Level C). (The background level is an order of magnitude lower at solar minimum.) For this reason, the Sun's output must be monitored and measured simultaneously with surface measurements, validating the need for a Solar X-ray Monitor (SXM) to be coupled with the REXIS instrument aboard OSIRIS-REx.

2.3. Technology of Operation: CCD-based Coded Aperture Imaging

The REXIS Instrument is being designed and developed as a CCD-based coded aperture telescope that relies on ray tracing and shadow casting to reconstruct spatial distribution of incident radiation. This section introduces the mechanism by which a CCD detector functions (Section 2.3.1) and basic limitations of CCD detector performance that are relative to this thesis (Section 2.3.2).

The ability to create a spatially accurate global map of elements at 1999 RQ36 relies on coded-aperture imaging. The system consists of:

(1) A coded mask – i.e., a plate with areas that are transparent or opaque to photons. The transport and opaque areas, 'mask elements', all have an equal size and are distributed in a pre-determined pattern, which is placed on a regular grid. The form of a mask element may be arbitrary.

(2) A position-sensitive detector, such as a CCD, whose spatial resolution is sufficiently matched to the mask-pattern grid size and which is sensitive to photons.

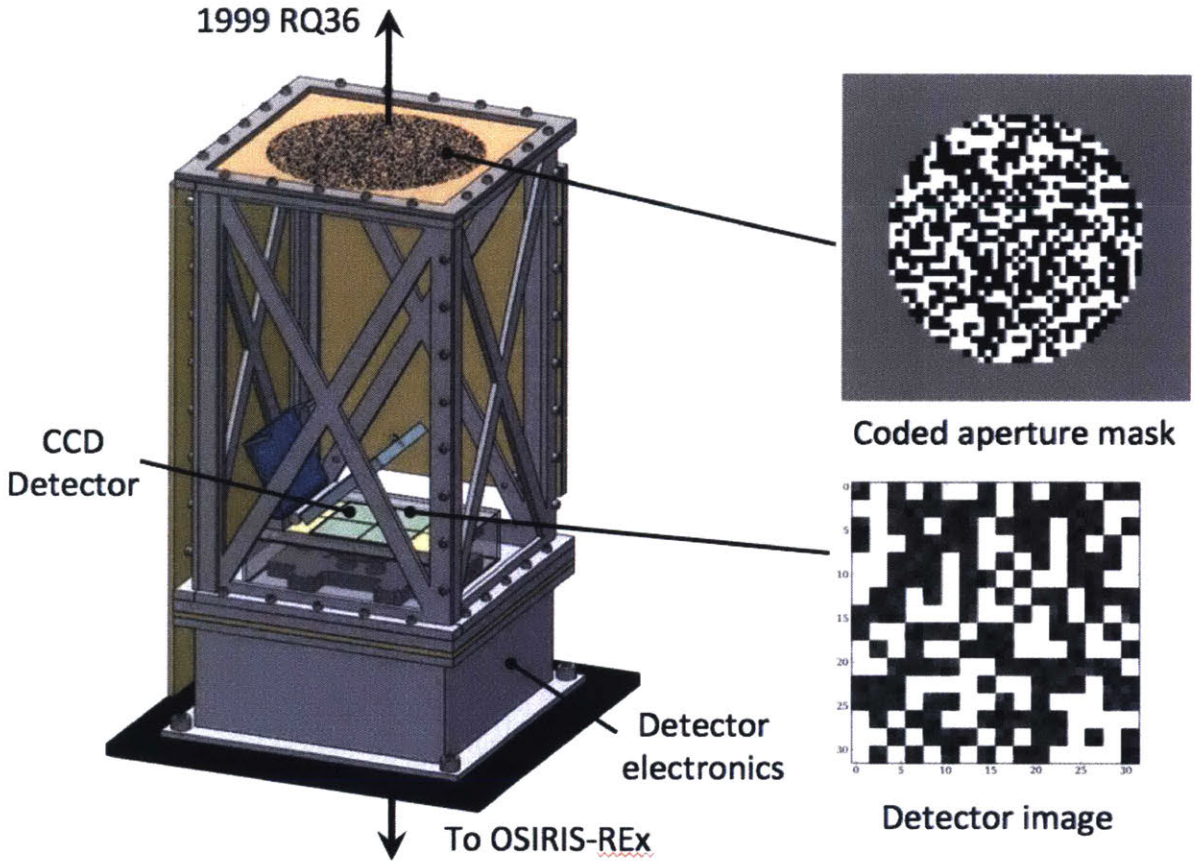

Figure 6: The REXIS open design mock-up depicting a coded aperture mask and detector image (MIT/Harvard Aperture & Detector Team, 2011).

As two point sources illuminate the detector through the mask, the detector records two projections of the mask pattern. The shift of each projection encodes the position of the corresponding point source in the sky; the 'strength' of each projection encodes the intensity of the point source.

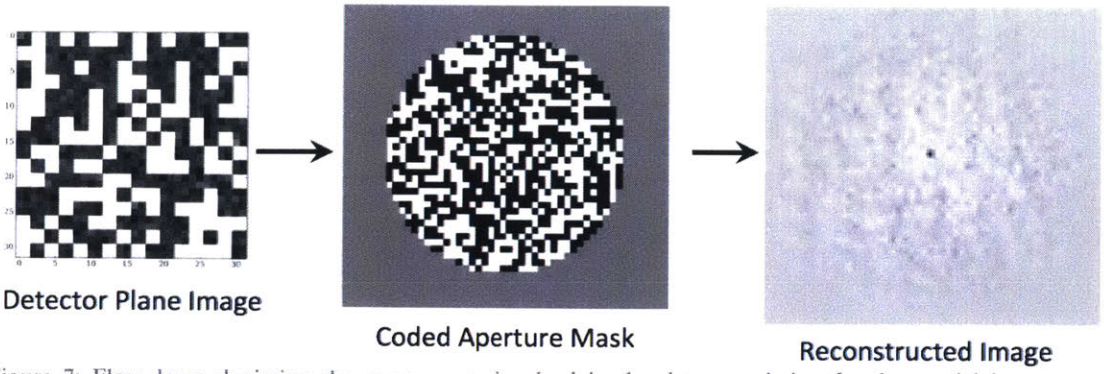

Figure 7: Flow-down depicting the components involved in the data correlation for the spatial image reconstruction process (MIT/Harvard Aperture & Detector Team, 2011).

The REXIS Instrument is being designed and developed as a CCD-based detector telescope relying on coded aperture imaging technology. Coded aperture imaging relies on simple ray tracing and shadow casting to reconstruct spatial distribution of incident radiation.

This thesis considers the factors in the CCD detector for efficient spectral resolution in order to attain useable scientific data in regard to spectral resolution. The following sections will discuss the foundations of CCD operations, CCD imaging inefficiencies, and related factors to imaging and how they will affect the REXIS Science product.

2.3.1. Introduction to CCDs

A CCD is a device for the movement of electrical charge, usually from within the device to an area where the charge can be manipulated, for example conversion into a digital value. This is achieved by "shifting" the signals between stages within the device one at a time. CCDs move charge between capacitive bins or potential wells in the device, with the shift allowing for the transfer of charge between the wells.

A CCD pixel consists of an SiO_2 layer on top of a Positive-type semiconductor.

CCD area detectors have a linear response to light and because CCDs store charge, from an electronics point of view, they are capacitors. Technically, a CCD is a Metal Oxide Semiconductor capacitor (MOS capacitor). CCDs employ "P-type" (Positive-type) semiconductors. Silicon has 4 e^- in its valance band, out of the total of 8 normally available valence sites. In a P-type semiconductor, "trivalent" impurities are added to Silicon to fill an additional 3 e^- sites. Thus, the existing 4 e^- + 3 e^- added = 7 e^- out of the 8 available valence sites. By missing one electron, the resulting Si has a positive charge.

An electrode, called a 'gate', at the top of the pixel 'bucket' applies a positive 'bias voltage.' The result is a 'potential well' to hold electrons. Each gate can transfer charge to its neighboring gate and are thus, "charge-coupled." Gates are inter-connected to transfer charge, even if the neighboring gate is in the next pixel. To read out a CCD, voltages are varied on each of the gates in a precise time sequence that transfers or 'couples' charge from one gate to another; in other words,

transferred from one potential well to another. The voltage sequencing of the gates that enables the transfer is called 'clocking the CCD.' Charge transfer efficiency (CTE) measures the efficiency of each pixel-to-pixel transfer, this transfer process is diagramed in Figure 8.

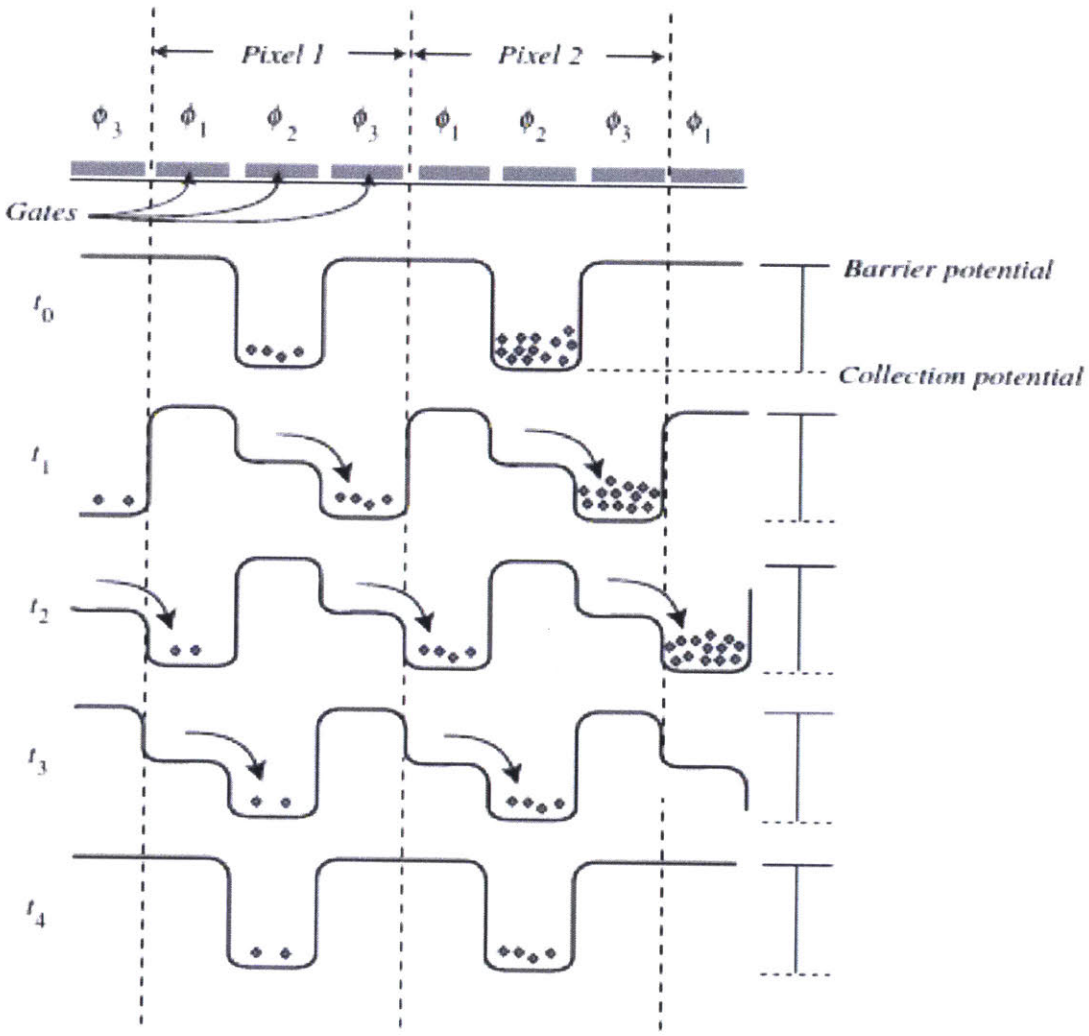

Figure 8: Shifting potential wells in a three-phase CCD. Two pixels in the same register (either parallel or serial) are illustrated here. At the end of the shift, electrons in pixel 1 have shifted to pixel 2 (Binzel, 2011).

These capacitors are biased above the threshold for inversion when image acquisition begins, allowing the conversion of incoming photons into electron charges at the semiconductor-oxide interface; the CCD is then used to read-out these charges.

From a report produced by Sternberg (2012), for X-ray CCDs, incoming X-rays strike the silicon surface of the CCDs. The impact from these energetic photon particles is capable of moving silicon valence electrons to the conduction band, where they are captured in the potential wells. Each X-ray

wavelength has an associated energy, and the higher the energy of the photon, the more electrons will be excited into the conduction band. Consequently, CCDs, are particularly useful in determining the elemental spectra of objects, including the asteroid 1999 RQ36, because each element fluoresces at a particular frequency and energy level. By allowing only one photon to hit a pixel before it is read out, i.e. the pixel charge is measured, it is possible to determine the energy of the incident photon, and there fore the element from which it was fluoresced, by counting the number of electrons in the pixel well (Howell, 2000). Although this process is highly efficient, noise is introduced at nearly every step in the detection-through-readout process.

The following section introduces CCD calibration requirements for effective performance of the processes outlined above.

2.3.2. CCD Detector Performance – Thermally Dependent Factors

CCDs are excellent detectors that require a great deal of calibration because they carry a variety of sources of noise. The detector's performance and resolution ability is greatly affected by its operating temperature and other smaller sources of noise. When imaging with CCDs a number of different types of calibration frames must be taken and applied to the science image(s) to remove these sources of noise and error to the scientific image frames.

The gain of a CCD is determined by the amplification performed by an on-chip amplifier that is built directly into the silicon circuitry (Sternberg, 2012). This amplification is defined as the amount of voltage required to produce one analog-to-digital (ADU) unit. The ADU converter converts the analog voltage reading to a digital number. A common method for determining the value to set as the gain is to relate the full pixel well capacity to the largest number that can be represented by the onboard analog/digital converter, provided that the CCD response is linear (Howell, 2000). CCD linearity means that the input charge varies linearly with the digital value of the output signal.

Readout noise is related to the gain, since it represents the number of electrons that are added per pixel into the final signal (Sternberg, 2012). These additional electrons do not originate from the incident X-ray photons, but rather from the process of the ADU converter and from the electronics that naturally introduce electrons throughout the imaging process (Pryor). The temperature of the CCDs and its thermal properties significantly affect the rate of non-photon generated electrons introduced. Because data processing takes place at for each pixel, read noise is added to each pixel at each readout time; consequently, each pixel has additional electrons added from readout noise each time the pixel is read (Howell, 2000).

Shot noise is related to the number of photons that are converted into electrons when they impact the CCD silicon, where the quantum efficiency is the primary temperature dependent factor in determining the shot noise. Since the quantum efficiency varies with temperature, it must be managed to ensure that the shot noise is low and that the spectral resolution meets REXIS requirements. Additionally, there is a shot noise specifically associated with X-ray CCDs that is related to the ability of the CCD silicon to interact with the incoming X-ray; if an incident photon does not interact with the silicon and instead passes through, then the CCD will be unable to read the energy of the photon and cause a loss of data (Howell, 2000). This noise is very small, however, as silicon's useful photoelectric effect ranges from 1.1 to 10 eV, which includes the soft X-ray region that REXIS measures.

Thermal effects are directly responsible for adding dark current noise. Because the CCDs are above absolute zero, a small number of electrons are able to escape from the valence band of the CCD silicon, becoming trapped in the potential well of the CCD pixels. These electrons create a Poisson noise distribution that must be filtered from the readout in order to separate the inherent dark noise from the image pixel by pixel (Janesick, 2001). Since the temperature of the CCD determines the thermal agitation and electron freeing potential, cooling the CCDs reduce the amount of dark current, making the thermal noise as low as possible by reducing the number of thermal electrons (Howell, 2000). It is additionally important to maintain the CCDs at uniform temperatures to prevent thermal changes across the CCDs that could artificially influence the readouts based on pixel location in the CCD array (Howell, 2000).

2.3.3. Spectral Degradation Due to Temperature

CCD performance depends on the detector's physical state which has a profound effect on the output scientific data. As CCD performance degrades our ability to measure spectral lines and distinguish neighboring lines from one another will degrade.

The temperature of CCDs is a crucial factor in the noise level seen in output data. Noise must be reduced or managed to achieve the required spectral resolution, thus temperature management is paramount. There are many factors of noise, the two most significant being the readout and dark current noises. Together, they form the majority of the total noise component in CCDs, so they are the two sources that are examined here (Sternberg, 2012).

The total noise N is defined as the following sum of the read and dark noises (Janesick, 2001):

$$N = \sqrt{\sigma_{read}^2 + \sigma_{dark}^2}$$

In this equation, the total noise is the square root of the sum of each noise component squared; the other forms of noise, such as shot noise, could similarly be added into this equation (Sternberg, 2012).

2.3.1.1. Readout Noise

The readout noise is proportional to the square root of the temperature and can be written as the following equation:

$$\sigma_{read}^2 = 4kTBR$$

In the above equation k is the Boltzmann constant of 1.38×10^{-23} J/K, T is the absolute temperature in Kelvin of the CCD, B is the noise power bandwidth in Hz, and R is the resistance of the

conducting path in Ohms (Janesick, 2001). The values *T, B,* and *R* are unknown values and are intrinsic to each CCD detector.

In order to determine the read noise as a function of temperature alone, values for *B* and *R* must be determined using existing data from flight heritage of the CCID-41 from the Suzaku mission. According to a paper by Bautz (2004), the read noise was measured on the Suzaku CCID-41s to be 2.5 e^- RMS at 41 kpix/sec and -90°C. Using these values for *T* and σ_{read}, the above equation can be solved for *BR*, yielding *BR* = 9.2029x10^{18}Hz-Ohms. Therefore,

$$\sigma_{read}^2 = 4 \times 1.38x10^{-23} \times 9.2029x10^{18} \times T$$

$$\sigma_{read}^2 = 5.08x10^{-4} \times T$$

This readout noise expression is shown graphically in Figure 9 below.

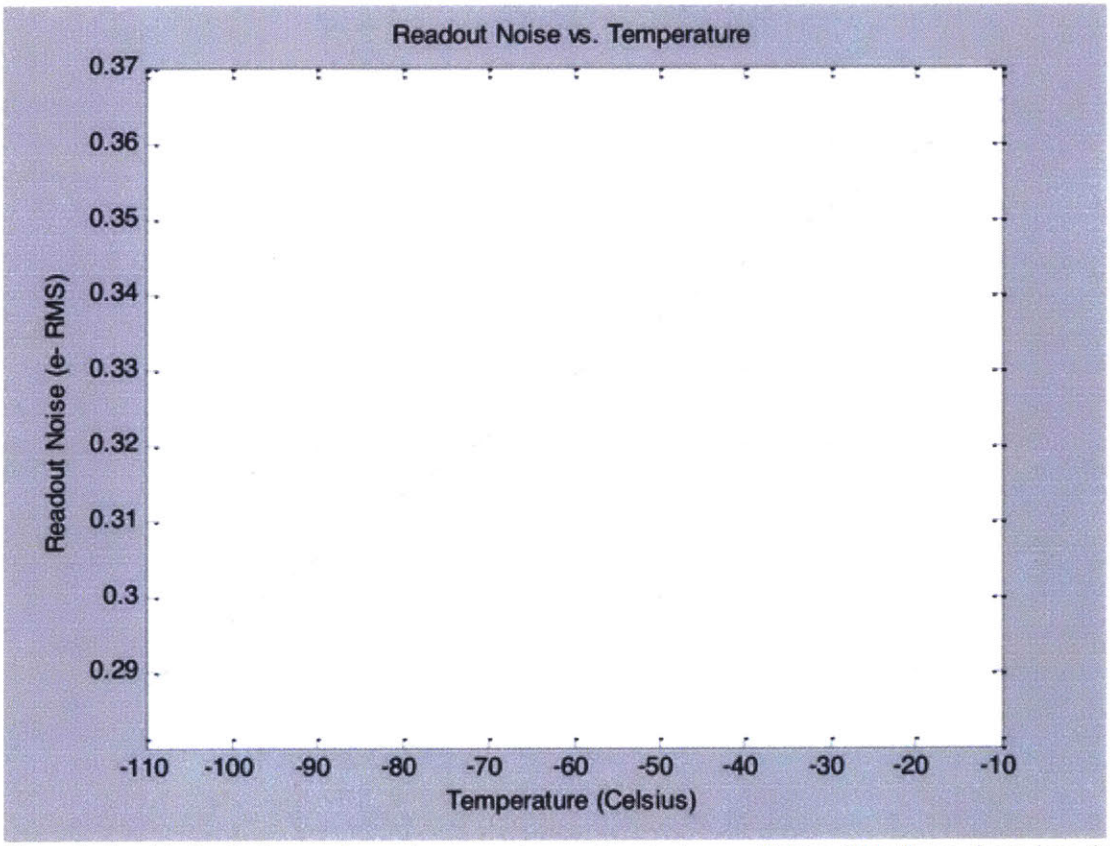

Figure 9: Graphically depicts readout noise versus temperature in degrees Celsius. This figure shows how the readout noise is affected by the CCD temperature. This linear relationship with temperature shows that the readout noise is best reduced at lower operating temperatures, showing the importance of cooled CCDs for improved spectral resolution (Sternberg, 2012).

The readout noise exhibits a linear relationship with temperature and is measured in e⁻RMS. Therefore, the readout noise contributes to the total noise expression values that vary linearly with the CCD operating temperature, with lower temperatures producing less readout noise. This noise must be removed with the subtraction of a dark image, i.e., am image where no X-ray sources are present, so that the readout noise is inherently part of this baseline frame (Janesick, 2001).

2.3.1.2. Dark Current Noise

The other major component of the total noise expression is the dark current noise, which is specific to each CCD.

The dark current noise is specific for each CCD, and is given for the CCID-41s as the following equation where T is temperature in Kelvin (Hamamatsu Photonics K.K.):

$$\sigma_{dark}^2 = 0.00092 \times T^{1.5} \times e^{-6995.35963/T} \left[\frac{A}{cm^2}\right]$$

Based on experimental data that is CCID-41 specific, conducted by the REXIS Science Team during the Summer of 2012, it is representative of exactly what is expected from the REXIS CCID-41s (Megyery, REXIS Science Team ETU-1: CCID-41 Laboratory Experimentation, 2012). The dark current noise is the largest component of the total noise of a CCD. Figure 10 shows a plot of this dark current noise. This noise source varies greatly with temperature, producing increasing noise with increasing temperature (Sternberg, 2012).

This dark current noise is shown graphically in Figure 10 below.

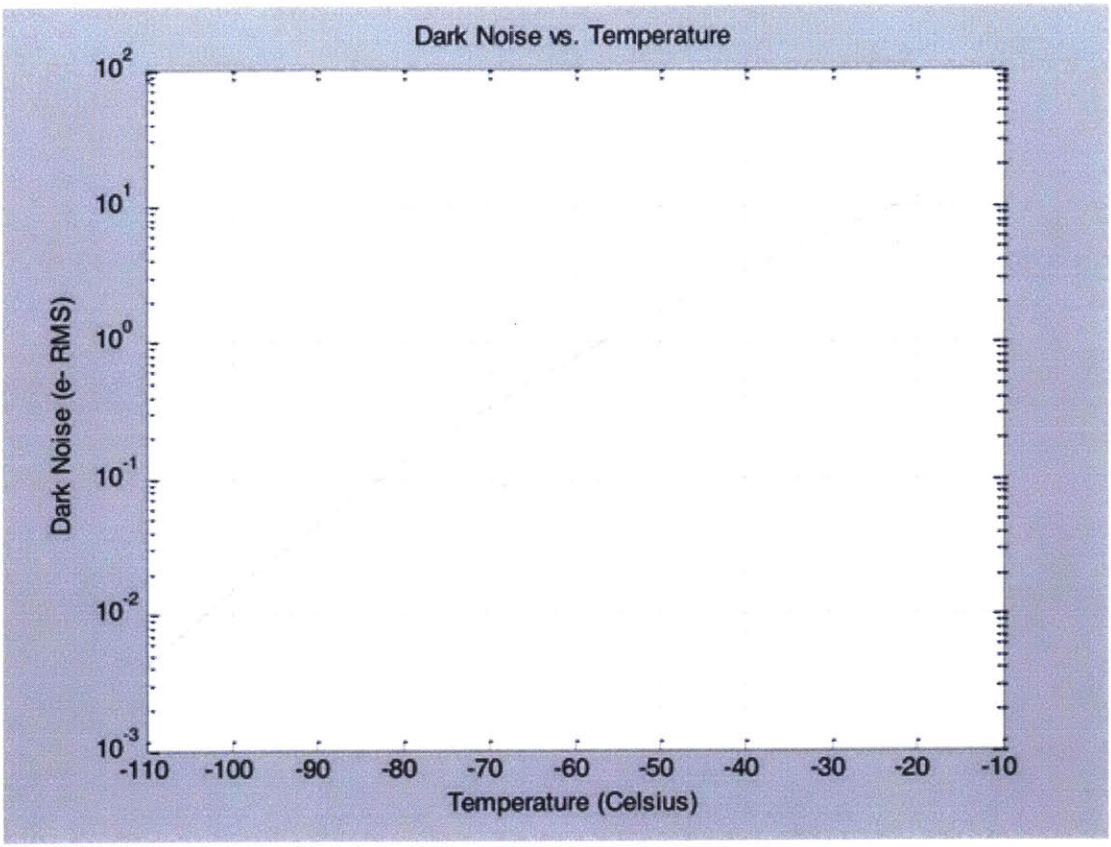

Figure 10: Graphically depicts dark noise versus temperature in degrees Celsius. This figure shows how the dark current noise varies as a function of CCD temperature. The low temperature regime shows markedly reduced dark noise, again showing the importance of cooled CCDs for improved spectral resolution (Sternberg, 2012).

2.3.1.3. Total Noise

As stated above, the total noise is the sum of several noise sources, most notably the readout and dark current noises. The analysis presented by Sternberg (2012) focuses on the larger magnitude sources of readout and dark current noises.

Figure 11 below shows a plot of the total noise as a sum of the readout noise (Figure 9) and dark current noise (Figure 10) sources, as derived in the total noise equation above.

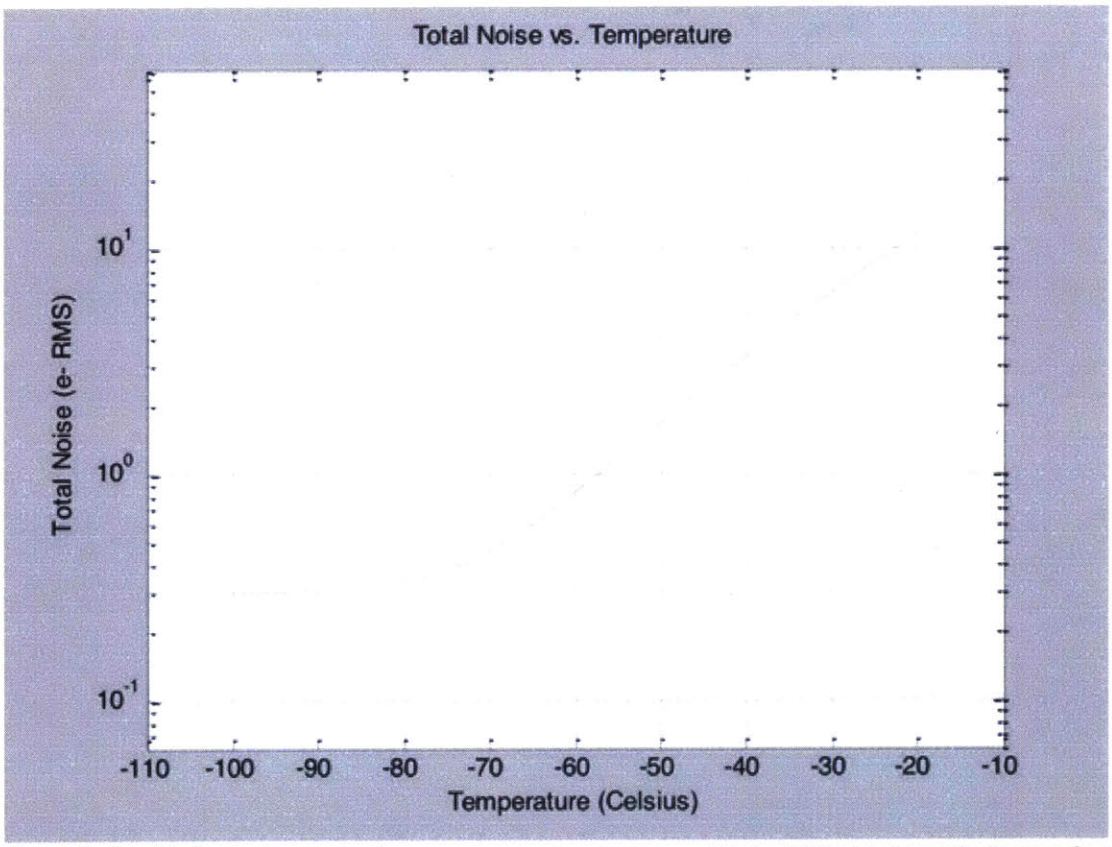

Figure 11: Graphically depicts total noise versus temperature in degrees Celsius. This plot shows the increase in total noise as a function of CCD temperature. The noise greatly increases with increasing temperature, especially above -75°C (Sternberg, 2012).

The total noise, here depicted as a sum of readout noise and dark current noise, is a crucial component in determining the instrument's spectral resolution.

2.4. CCD-based XRF Detection

2.4.1. CCDs for X-ray Fluorescence

To gather information from a CCD area detector we count the electrons that are collected in each potential well.

When an X-ray photon comes into the CCD detector and interacts with the silicon, that X-ray gets converted into electrons. For an X-ray with a particular energy you assume that all of that energy gets converted into an equivalent number of electrons.

On the smallest level, an incoming photon to the semiconductor will hit an atom and excite it. The atom is now in an excited state and can kick out an electron and is now a positive ion, which we call a hole, with an electron floating around. This electron-hole pair is called an exoton. This exoton is where the information is and it must be captured before it is lost, because all exotons end up being recombined.

In example, for an X-ray with 1keV energy it gets converted and produces an average energy of 3.65eV/electron. Thus, for a 1keV photon:

$$\frac{1000eV}{3.65eV/electron} \cong 273electrons$$

This cloud of charge gets collected and converted in the CCD, with a certain conversion gain, that gives the number of Analog/Digital Units (ADUs).

For example, Fe55 has two peaks in its spectrum – the kα at 5.9keV and kβ at 6.4keV. From these energies we can compute the number of electrons that are excited when a kα or kβ X-ray photon interacts, respectively:

$$\text{Fe55 k}\alpha \quad \frac{5900eV}{3.65eV/electron} \cong 1616electrons$$

$$\text{Fe55 k}\beta \quad \frac{6400eV}{3.65eV/electron} \cong 1753electrons$$

This may seem like a large number of electrons, but in fact, the well-depth of CCDs can be anywhere from 50,000 to 150,000 electrons. The well-depth of a CCD dictates the number of electrons it can collect in a pixel before it starts to spill over into the next pixel. So this is actually a very narrow range of ADUs in the system.

2.4.1.1. Point Source Imaging

Some X-ray events will land neatly in one pixel and these are referred to as grade-zero events. In these cases, the electrons that come in all get deposited on one pixel meaning there is total charge collection. In this case, the kα and kβ peaks will show up as very sharp lines.

Occasionally there will be splits, where an event lands between pixels and the energy from that X-ray event is transferred into two, or more, neighboring potential wells. Say, for example, that ¾ of the event falls in one pixel and ¼ of the event falls in another. In this case, the kα peak will have two energies and so the net effect is that the histogram will not show one sharp line. In this case we will simply sum the electrons from both pixels for that event. For this reason, we must always first find the centroid of each X-ray event.

Since X-ray events are small and sparse on a CCD area a 3x3pixel area is margin enough to center around any particular X-ray event. Thus, summing up all the electrons in that 3x3 box of pixels will give the count value of that particular event.

However, XRF imaging of a planetary body is not point-source imaging but rather continuous source imaging.

2.4.1.2. Continuous Source Imaging

Continuous source imaging can be considered a massive integration of point sources all interacting with the CCD continuously upon the detector area. There will no longer be clean peaks and clean, sparse X-ray events in an otherwise blank field. The conditions when imaging Asteroid 1999 RQ36 will be that of many elements fluorescing X-rays at the REXIS CCD detector all immediately next to each other. To properly analyze this area in order to determine what elemental peaks are present in our continuous spectrum will take some mastery and familiarity.

In this case, a simple 3x3 pixel box size will not be sufficient. There will be a certain surface resolution that will need to be optimized against a certain spatial resolution in order to be able to distinguish individual peaks within a spectrum within an area of pixels. This will be discussed in detail in Section 3.1.

2.4.2. Spectral Resolution FWHM

The spectral resolution full-width half-maximum (FWHM) can be expressed as (Janesick, 2001):

$$\Delta E_{FWHM} = 2.345 \times 3.65 \sqrt{N^2 + \frac{FE_x}{3.65}}$$

In this equation the FWHM is measured in eV, the 2.345 term models the Gaussian distribution of the spectral resolution, 3.65 is measured in eV/e^-, F is the Fano Factor, or 0.1 for silicon, and both

N and E_x are measured in e^-, since they represent the number of electrons of noise and the number of electrons produced for an X-ray with energy E_x, respectively (Sternberg, 2012).

By combining the FWHM equation with the expressions for read noise, σ_{read}, and dark current noise, σ_{dark}, one can derive an expression relating the FWHM spectral resolution as a function of temperature and incoming X-ray energy. The resulting expression is:

$$\Delta E_{FWHM} = \sqrt{0.0372T + 2.4264x10^{12}T^{1.5}e^{-6.9954x10^{3}T} + 2.0074E}$$

The above expression has only one term dependent on the energy, E, and two terms dependent on temperature, T. This expression allows for the maximum noise to be found for a given X-ray energy to meet a particular FWHM spectral resolution requirement. Consequently, the REXIS requirement REX-3.1.1 can be expanded to include the maximum noise permitted in order to abide by the spectral resolution requirements.

Table 5: Maximum noise levels associated with REXIS spectral resolution requirements.

FWHM (eV)	X-ray Energy (keV)	Maximum Noise (e^- RMS)
<80	0.5	8.58
<100	1	10.45
<120	2	11.91
<150	4	14.05
<200	6	19.53

(Sternberg, 2012)

It is clear from Table 5 that the noise levels that are required to meet and exceed the FWHM requirements are well above any of the noise levels seen through the analysis and graph shown in Figure 11. Therefore, the noise levels expected from theoretical results are well below the levels at which the FWHM requirements would be exceeded (Sternberg, 2012).

In the spring of 2012 the REXIS Science Team (Megyery, REXIS Science Team; ETU-1: CCID-41 Laboratory Experimentation) conducted radiation measurements of a CCID-41 with an ^{55}Fe point source to allow the team to model CCD energy resolution performance at 6 keV as a function of temperature.

To correlate the data from the analytical model conducted by Sternberg (2012) with the experimental data, from the experiment designed by Megyery and the REXIS Team (2012) and conducted by the MIT/Harvard REXIS Science Team (2012), the two sets of data were plotted together.

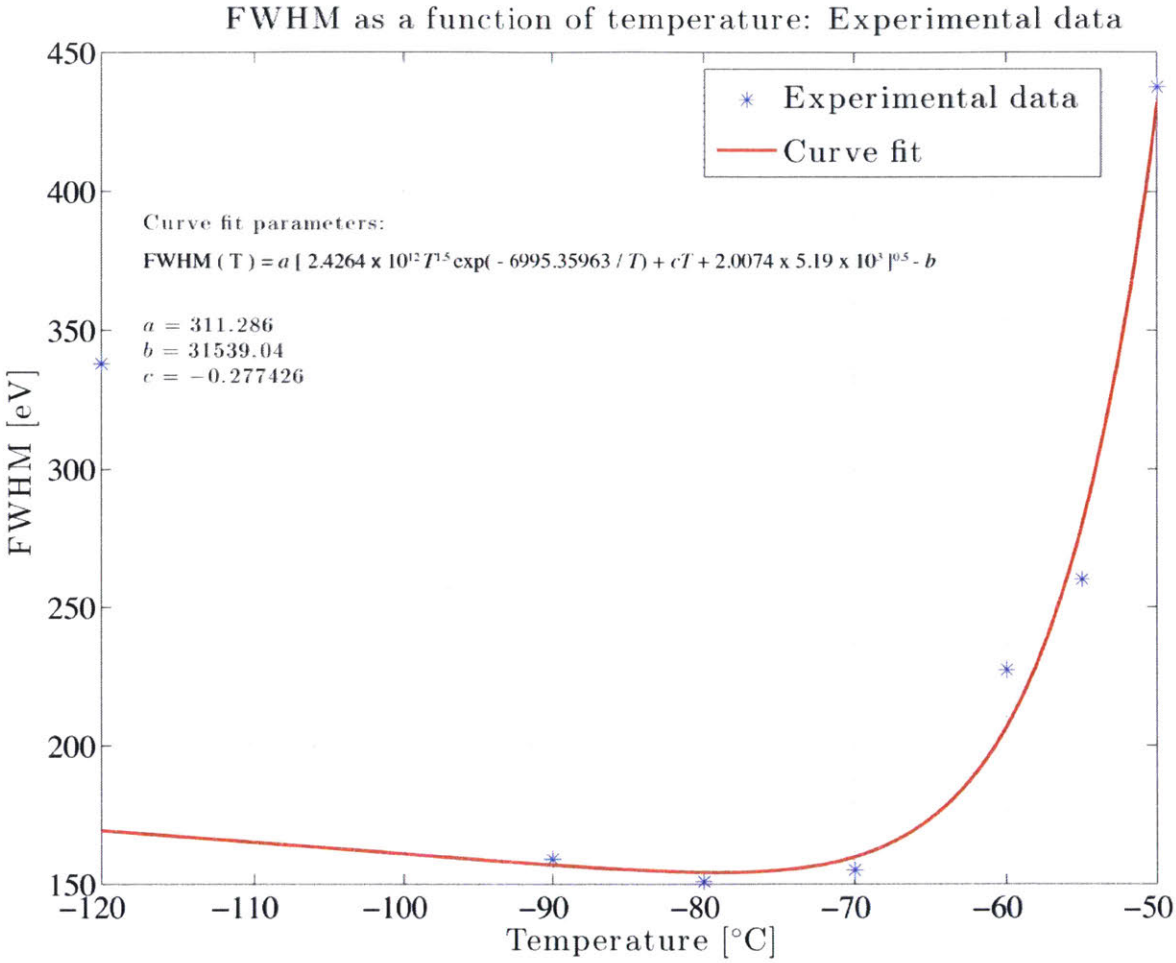

Figure 12: Graphical results of the correlation of the analytical model by Sternberg (2012) with the experimental data of the CCID-41, from the experiment designed by Megyery and the REXIS Team (2012) and conducted by the MIT/Harvard REXIS Science Team (2012). The experimental result data was fitted with a curve that distinctly shows the FWHM of the detected elemental line significantly increases at detector temperatures above -75°C (Image Credit: Inamdar, 2013).

The experimental data results agree with the graphical result for total noise that above -75°C the FWHM [eV] sharply increases and goes beyond the REXIS requirement thresholds. This result on the FWHM as a function of temperature is simply based on the readout noise and dark current noise, both intrinsic to the detector. In order to determine the upper bound on CCD operating temperature, the FWHM must be analyzed as a function of temperature. By varying the temperature in the FWHM equation above until the REXIS requirement is exceeded, it is possible to determine this upper temperature bound. However, an additional parameter that increases the FWHM of spectral lines is the cross-contamination of neighboring lines which alter the specific energy intensity that is read out by the CCD and directly affect the accuracy requirement set forth for REXIS in REX-2.1.1. Both of these requirements must be met and the method for this analysis and results is discussed in Chapter 3.

Chapter 3: Investigation of Spectral Resolution Limits

3.1. Theoretical Global Model for X-ray Line Production

Fluorescent X-rays characteristic of major elements are produced when solar X-rays with energies greater than the energy of the line itself bombard a surface. One group of lines produced in this way, known as K α lines, are those that result from processes that occur in the innermost K-shell. The K-shell absorption edge of an atom is the binding energy of its innermost electron shell. The energies of K-shell absorption edges for major elements on interests (Fe, Ti, Ca, Si, Al, and Mg) are in the soft X-ray region of interest (P. Clark J. T., 1997). In order to eject a K-shell electron from an atom through photo-absorption, thereby causing the emission of a fluorescent K α X-ray, incident X-rays must have energies greater than K-shell binding energy. Thus, only X-rays with energies greater than the energy of the K-edge, and greater than the energy of the fluorescent line as well, are capable of exciting that element. Increasing the intensity, or level of the source, meaning increasing the level of solar activity, translate into the achievement of better statistics, shorter integration times, and hence higher resolution maps. As a consequence of the inverse relationship between solar energy and output, production of the higher energy XRF lines for the heavier elements is significantly reduced relative to the production of lines for lighter elements. Thus, longer integration times are required to achieve the same levels of sensitivity for the heavier elements. Longer integration for orbital data results in inherently lower spatial resolution, as well.

3.1.1. X-ray Fluorescence Equation

The method for calculating the X-ray fluorescence for the K α line for each element, as well as the coherent and incoherent scatter in the vicinity of the line (determined by integrating the output flux across the line's full width at half maximum as determined by its resolution) is presented in Clark and Trombka (P. Clark J. T., 1997).

The following equation gives the relationship used to model fluorescent line production, I_F, for each element of interest (R. Jenkins, 1967; Clark, 1979).

$$I_F = \omega_j g_j \frac{r_j^{-l}}{r_j} \frac{d\Omega}{4\pi} \frac{C_j}{D_j} \int_{\lambda_{min}}^{\lambda_{edg}} J(\lambda) \cos\alpha \frac{\mu_j(\lambda)}{\sum_{i=1}^{N} \left[\mu_i(\lambda) + \mu_i(\lambda_j) \frac{\cos\alpha}{\cos\beta}\right]} d\lambda$$

Table 6: Definition of model parameters used to model fluorescent line production

Term	Definition	Description
i	All elements (major) being considered	
j	Fluorescing elements only	
D	Square of the distance in AU	
J	Primary source flux	Least squares fit to observed spectra
μ_i	Energy absorption efficiency of i elements	Power law functions of i
μ_j	Energy absorption efficient of j elements	Power law functions of j
C_i	Concentration for each element in matrix	Soil averages
C_j	Concentration for fluorescing element	Soil averages
$d\Omega$	Angular distribution term	(Detector area) (Surface area) / (Altitude^2)
α	Complement of incident flux angle	0° at subsolar point
β	Complement of exiting flux angle	0° for nadir pointing instrument
ω_j	Kα line fluorescence yield	Constant for each element
r_j	Jump (K-shell absorption) ration	Constant for each element
g_j	K-shell hole transfer probability	Always 1 for K-shell
λ_{min}	Starting integration wavelength	Empirically lowest measureable flux
λ_{edg}	Ending integration wavelength	Absorption edge

(Clark, 1979)

The fluorescent flux is calculated by integrating over a range of wavelengths, λ_l, from a minimum wavelength above which fluorescence is empirically determined to become negligible to the absorption edge. The Sun's soft X-ray output, variable J, is calculated as a function of energy with a polynomial least squares fit to published estimates of solar output as shown in Table 2 (P. Clark J. T., 1997). The strength of the source, J, depends on the complement of the incident flux angle of the source, α; thus, J is multiplied the cosine of α. Power laws, as shown in ST2, are used to describe an element's X-ray photoabsorption capability, μ, as a function of energy (Clark, 1979; Hubbell, 1969). The series of power laws that predict photoabsorption for each element each apply within the wavelength limits indicated, the limits representing absorption edges for that element. The mass absorption, μ_i, of the fluorescing element, j, is directly related to its fluorescence intensity. C_i is the concentration of the fluorescing element. The mass absorption, μ_i, by other elements, i, which are major components of the surface with concentrations C_i, is inversely related to mass absorption at each wavelength, μ_i, and to fluorescence at the wavelength of the chosen line, μ_i. The ratio between the complements of the arriving flux angle, α, and the departing flux angle, β, is also part of the mass absorption term. When REXIS is nadir-pointing, the complement of the departing flux angle, β, is always $0°$.

Table 7 shows the value of X-ray production parameters for the elements considered across REXIS' range. Fluorescence yield, jump ratio (K-shell absorption probability), and K-shell hole transfer factor are all probability factors associated with given elements. Fluorescence yield systematically improves as the atomic weight increases. The energy angular distribution term depends on the relationship between the detector area and footprint area, which itself depends on the altitude and angular field of view of the detector.

Table 7: X-ray production parameters for elements considered in calculations

Element	Atomic Number	Atomic Weight	Absorption Edge λ_{edg}	$K\alpha$ Line j	Jump Ratio r_j	Fluorescence Yield ω_j	Mass Absorption (λ in A) Power Law	Power Law
Ni	28	58.7	1.49				$113.0(\lambda^{2.75})$ @ $0 < \lambda < 1.49$	$15.3(\lambda^{2.75})$ @ $1.49 < \lambda < 12.3$
Co	27	58.9	1.61				$100.0(\lambda^{2.78})$ @ $0 < \lambda < 1.61$	$13.6(\lambda^{2.63})$ @ $1.61 < \lambda < 13.4$
Fe	26	55.9	1.74	1.94	8.1	0.342	$95.3(\lambda^{2.66})$ @ $0 < \lambda < 1.74$	$13.2(\lambda^{2.59})$ @ $1.74 < \lambda < 14.7$
Mn	25	54.9	1.90				$86.0(\lambda^{1.90})$ @ $0 < \lambda < 1.90$	$11.4(\lambda^{2.63})$ @ $1.90 < \lambda < 16.1$
Cr	24	52.0	2.07				$76.0(\lambda^{2.69})$ @ $0 < \lambda < 2.07$	$10.6(\lambda^{2.58})$ @ $2.07 < \lambda < 17.9$
Ti	22	47.9	2.50	2.75	9.1	0.221	$61.3(\lambda^{2.34})$ @ $0 < \lambda < 2.50$	$7.93(\lambda^{2.63})$ @ $2.50 < \lambda < 22.0$
Ca	20	40.1	3.07	3.34	8.6	0.163	$52.3(\lambda^{2.69})$ @ $0 < \lambda < 3.07$	$7.79(\lambda^{2.53})$ @ $3.07 < \lambda < 28.3$
K	19	39.1	3.44				$43.9(\lambda^{2.75})$ @ $0 < \lambda < 3.44$	$5.50(\lambda^{2.61})$ @ $3.44 < \lambda < 21.5$
S	16	32.1	5.03	5.37	10.3	0.082	$27.5(\lambda^{2.75})$ @ $0 < \lambda < 5.03$	$2.85(\lambda^{2.72})$ @ $5.03 < \lambda < 18.5$
P	15	31.0	5.79				$22.2(\lambda^{2.75})$ @ $0 < \lambda < 5.79$	$2.23(\lambda^{2.75})$ @ $5.79 < \lambda < 15.5$
Si	14	28.1	6.75	7.12	11.2	0.044	$19.9(\lambda^{2.84})$ @ $0 < \lambda < 6.75$	$2.78(\lambda^{2.55})$ @ $6.75 < \lambda < 45.0$
Al	13	27.0	7.96	8.34	11.9	0.038	$14.3(\lambda^{2.83})$ @ $0 < \lambda < 7.96$	$1.90(\lambda^{2.67})$ @ $7.96 < \lambda < 45.0$
Mg	12	24.3	9.51	9.89	12.8	0.030	$11.4(\lambda^{2.80})$ @ $0 < \lambda < 9.51$	$1.60(\lambda^{2.56})$ @ $9.51 < \lambda < 45.0$
Na	11	23.0	11.6				$8.00(\lambda^{2.95})$ @ $0 < \lambda < 11.6$	$1.24(\lambda^{2.50})$ @ $11.6 < \lambda < 45.0$
O	8	16.0	23.3				$2.95(\lambda^{3.00})$ @ $0 < \lambda < 9.6$	$10.9(\lambda^{2.48})$ @ $9.60 < \lambda < 23.3$
C	6	12.0	43.7				$1.24(\lambda^{3.06})$ @ $0 < \lambda < 18.0$	$8.00(\lambda^{2.36})$ @ $18.0 < \lambda < 45.0$

(Clark, 1979)

In other terms, if E is the X-ray energy and the incident intensity of parallel solar X-rays on the surface of an atmosphereless body is $I_0(E)$ (photons cm^{-2} s^{-1}) then the intensity of fluorescence from a given X-ray line (photons cm^{-2} s^{-1} $steradian^{-1}$) can be determined in terms of fundamental physical parameters by the relationship shown in the following equation, adapted from Clark and Trombka (P. Clark J. T., 1997; G. W. Fraser, 2010).

$$I_{line} = \frac{1}{4\pi}\omega_i g C_i \left(\frac{r-1}{r}\right) \int_{E_{abs}}^{\infty} I_0(E)\rho \cos\theta \frac{\left(\mu(E)_i/\rho_i\right)}{\mu(E) + \mu(E_{line})\left(\cos\theta/\cos\phi\right)} dE$$

Table 8: Defines each of the model parameters in the X-ray Fluorescence Line Intensity equation above

Term	Definition
ω_i	Fluorescence yield of a given emission series (K, L, etc.)
g	Weight fraction of a given line within a series (α, β, etc.)
C_i	Mass fraction of a given element
r	Jump ratio at the absorption edge of interests
ρ	Bulk density of the surface material
ρ_i	Partial density of the element of interest
θ	Angle of incidence of the incident solar X-rays, measured from the surface normal
ϕ	Viewing angle measured from the surface normal
$\mu(E)$	Mass absorption coefficient of the bulk material
$\mu(E)_i$	Linear absorption coefficient for the element of interest
E_{line}	Energy of the elemental emission line of interest

(P. Clark J. T., 1997)

The equation above also assumes a perfectly smooth and homogeneous planar surface; no allowance is made for effects due to the real properties of the regolith, including surface roughness and packing density. Also unaccounted for are shadowing effects due to large-scale topography. According to Fraser, et al. (G. W. Fraser, 2010), energy independent effects of the regolith and topography (e.g. shadowing) may be removed by the use of elemental abundance ratios (e.g. Mg/Si, Al/Si) instead of absolute abundances, however the use of ratios cannot remove any effects for which there is an energy dependency, and it has been shown in preliminary measurements that for large values of θ and ϕ the measured ratios of elemental line intensities varies as a function of surface roughness by 10-20% (J. Naranen H. P., 2007; J. Naranen H. P., 2008). These effects are mentioned in Appendix B.2. Work is continuing at the University of Leicester, the University of Helsinki and Birkbeck College to quantify the effects of regolith properties on line intensities, in order to provide a more complete interpretation of X-ray fluorescence data from planetary surfaces (G. W. Fraser, 2010).

3.2. Developing Inputs for Spectral Resolution Modeling

Spectral resolution modeling determined and verified the detector requirements for temperature, spectral resolution, quantum efficiency, by their relation with accuracy of line ratio measurements (accuracy requirement of 10%). The spectral modeling also determined the spectral contamination of each X-ray fluorescent line. The results of the spectral modeling will be used to provide an estimate for photon counts of each X-ray fluorescent line, which can be used for input of imaging and collimation simulation and analysis.

As introduced in Chapter 2, CCD performance depends on the detector's physical state which has a profound effect on the output scientific data. As CCD performance degrades our ability to measure spectral lines and distinguish neighboring lines from one another will degrade. CCD noise depends primarily on (1) the Energy of the incident radiation and (2) the Temperature of the CCD. In order to meet REXIS requirements REX-2.1.1 and REX-3.1.1 these values need to be quantitatively analyzed and the CCD temperature limit needs to be set in order to meet the 10% accuracy of the incident energy measurement requirement. Experimentation results for the CCID-41 yielded FWHM as a function of detector temperature (Figure 12). Chapter 2 also introduced that noise is dependent on incident X-ray energy and CCD temperature.

3.2.1. Model Input Development

Using the model solar spectrum minimum/quiet solar state (Figure 3) (Lucy Lim, 2012) as a guide, the ideal Class-A X-ray solar spectrum was derived by Allen (2012) and is shown in Figure 13.

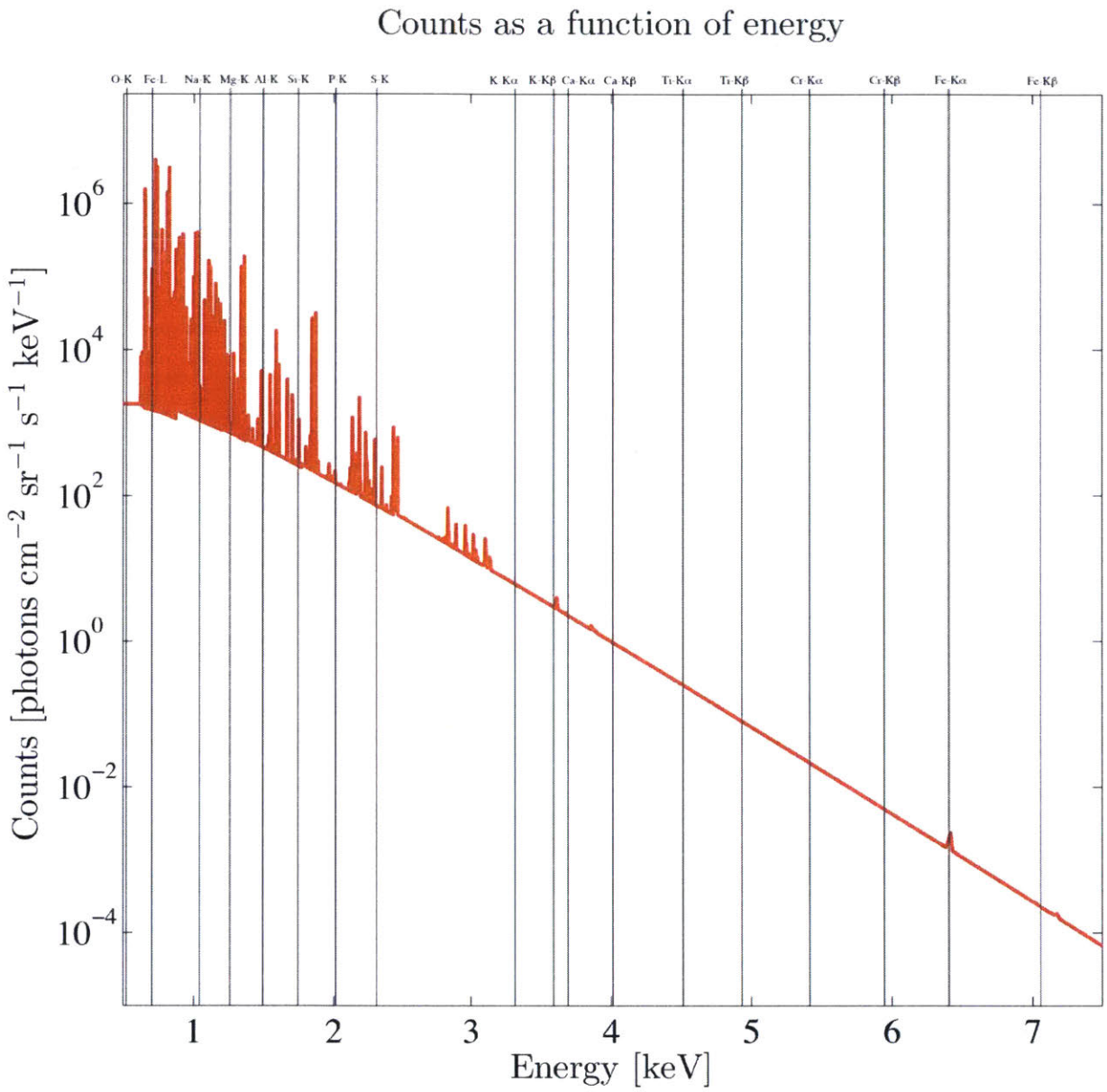

Figure 13: Ideal solar spectrum for Class-A solar flare state used as input into the XRF Equation. REXIS elemental lines of interest are vertically marked on the graph. This ideal solar spectrum was used as input into the XRF equation to generate the ideal chondrite X-ray spectrum for a Class-A solar state (Image Source Credit: Allen, 2012; Image Source Edit: Megyery, 2013).

Figure 13 shows the ideal solar spectrum for Class-A solar flare state and was used as the input solar spectrum into the XRF Equation to yield the ideal chondrite spectrum as shown in Figure 14.

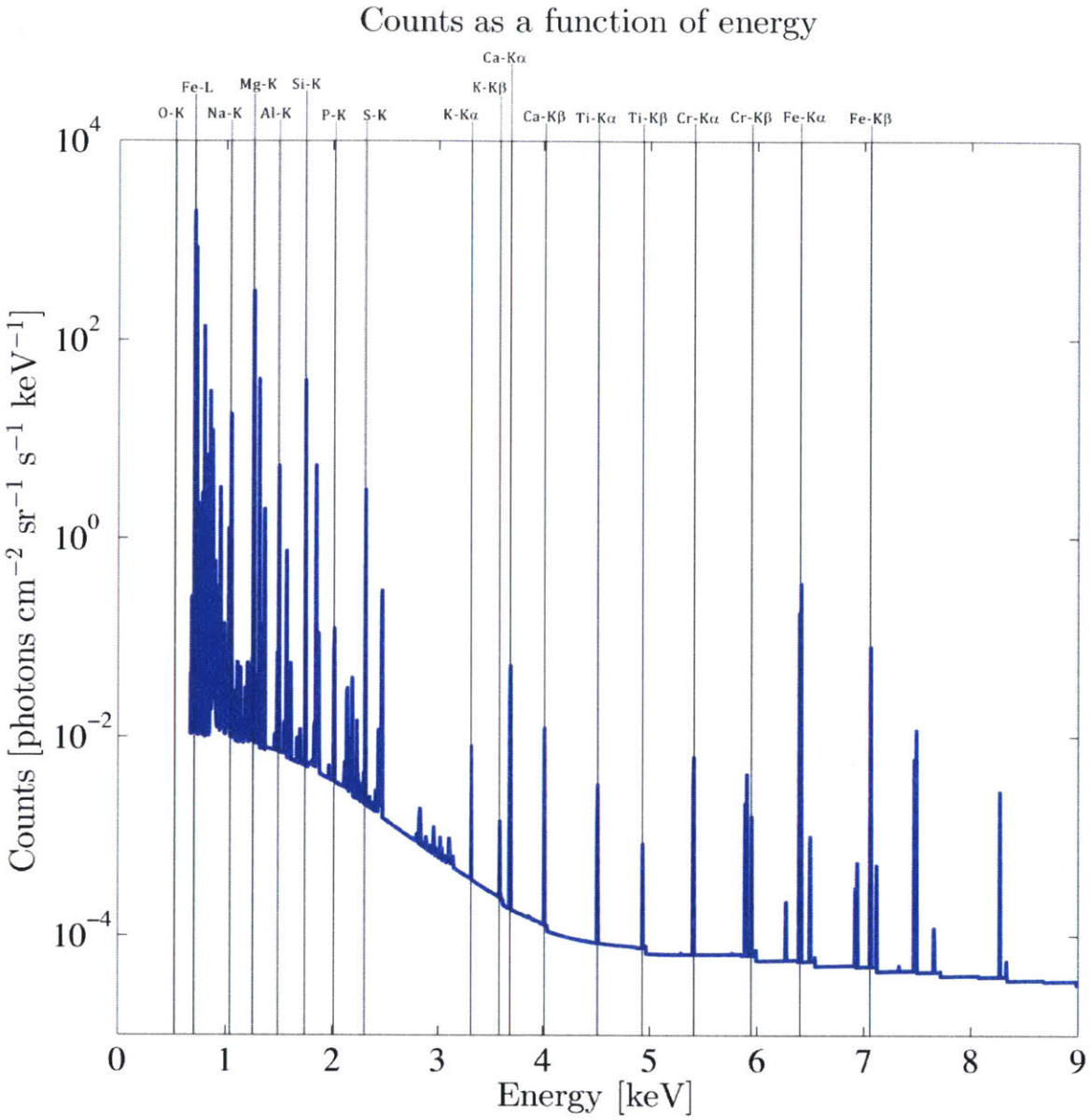

Figure 14: Ideal chondrite spectrum for Class-A solar flare state as output from the XRF Equation. REXIS elemental lines of interest are vertically marked on the graph. This spectrum does not include any noise effects that would affect the FWHM of lines or the contamination of counts from neighboring lines (Image Source Credit: Allen, 2012; Image Source Edit: Megyery, 2013).

Figure 14 shows the ideal solar spectrum for Class-A solar flare state and was used as the input solar spectrum into the XRF Equation to yield the ideal chondrite spectrum. This ideal chondrite spectrum is used as input into the spectral resolution model to be discussed in Section 3.3.

3.3. Spectral Resolution Modeling

The full spectral resolution model results define the necessary CCD conditions to meet the REXIS accuracy requirement REX-2.1.1 and the spectral resolution requirement REX-3.1.1; the model has two main inputs. The first input is the results of the CCID-41 laboratory experiment (Figure 12), accounting for the intrinsic detector properties contributing noise to the spectrum. The second input is the ideal chondrite spectrum (Figure 14), developed from the Class-A solar flare state which is the expected state when REXIS encounters 1999 RQ36. These two inputs are then put into the spectral resolution model to generate a more accurate looking spectrum with Gaussian-like peaks, unlike the ideal chondrite spectrum (Figure 14). These peaks are then broadened in the model until the model 'breaks' and neighboring peaks are no longer discretely discernible.

3.3.1. Curve Contamination and Measurement Accuracy Requirement

As has been discussed earlier, the FWHM of spectral lines is not only dependent on CCD detector noise. To mitigate this, REXIS has line measurement accuracy requirement of 10%. This section graphically and quantitatively defines the derivation of this 10% accuracy requirement.

Unfortunately, due to intrinsic detector noise, the X-ray detection results of REXIS will not be sharp, distinct peaks as shown in the ideal chondrite spectrum of Figure 14. Rather, we will see Gaussian shaped lines centered about a specific Energy value with a peak Intensity. As many of these lines are very near each other, the counts from one line will contaminate the counts of neighboring lines as outlined in the following model developed by Inamdar (2013).

The model begins by choosing a width or region of interest about a peak; this width can be chosen arbitrarily, but is typically at FWHM. Let this total width be given by $2\varepsilon_i$ for line i. We are in principle calculating how many counts are contaminated between adjacent lines. For two lines, ideally, heights of $I_{0,1}$ and $I_{0,2}$, the actual distribution will be, due to line broadening from natural effects and detector effects, $I_1(E)$ and $I_2(E)$. The associated peak energies are given by $E_{0,1}$ and $E_{0,2}$.

The contamination from one line i into the line j, C'_{ij} into the other is given by:

$$C'_{1,2} = \int_{E_2-\varepsilon_2}^{E_2+\varepsilon_2} I_1 dE$$

$$C'_{2,1} = \int_{E_1-\varepsilon_1}^{E_1+\varepsilon_1} I_2 dE$$

The contribution from line i to itself is given by:

$$C_i = \int_{E_i-\varepsilon_i}^{E_i+\varepsilon_i} I_i dE$$

A graphical representation of this contamination of counts of neighboring lines is given in Figure 15 below.

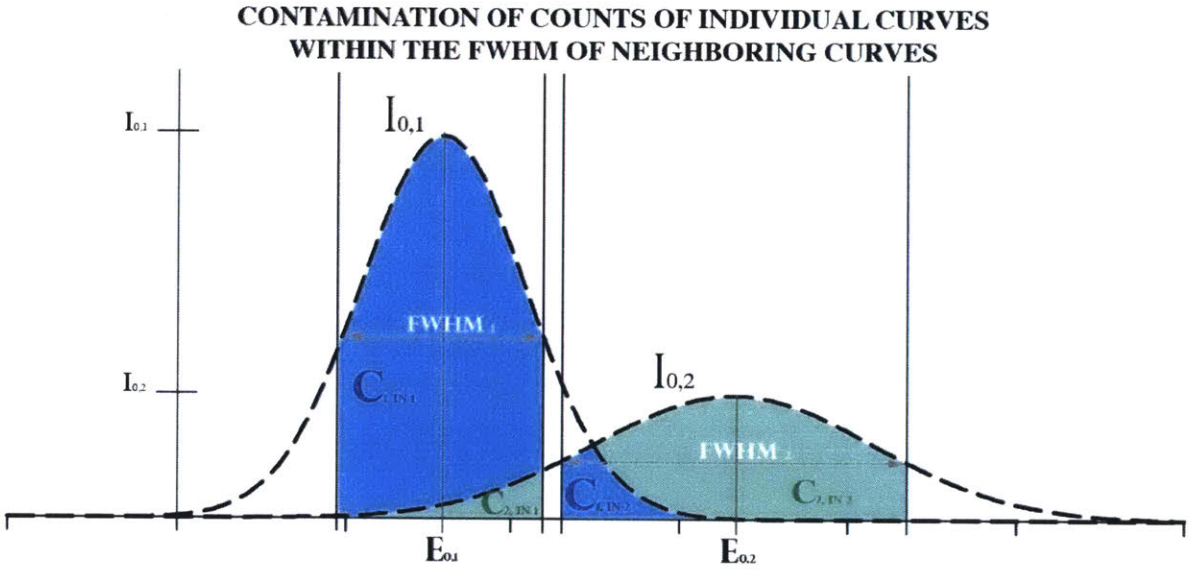

Figure 15: Graphical depiction of curve contamination of counts of individual curves within the FWHM of neighboring curves. In this graphic the curve's FWHM is used as the region of interest about the peak and the differently shaded regions in each show the contamination from Curve 1 in Curve 2 and Curve 2 in Curve 1. The spectral resolution model described in this section provides the quantitative solution to accounting for this contamination in order to meet the accuracy requirement set for REXIS (Image Credit: Megyery, 2013).

To determine the acceptable spectral resolution, we pick two lines and form widths (usually the FWHM) around these peaks. We know the ideal line heights, and, in the perfect case, will want to measure the ratio of the heights $I_{0,2}/I_{0,1}$. What, in reality, we will have are measurements of the contamination as above:

$$C_{1,total} = C'_{2,1} + C_1$$

$$C_{2,total} = C'_{1,2} + C_2$$

The accuracy, η, is then set by comparing the actually measured counts (with contamination) with the ideal line ratios:

$$\left|\frac{I_2/I_1}{(C'_{1,2}+C_2)/(C'_{2,1}+C_1)}\right| = 1+\eta$$

We require, then, that:

$$\left|\frac{I_2/I_1}{(C'_{1,2}+C_2)/(C'_{2,1}+C_1)}\right| - 1 < \eta^*$$

Where η^* is the accuracy as determined by the REXIS requirements, according to requirement REX-2.1.1 that accuracy is 10%.

For reference, the $K\alpha$ Line energy value in keV and the FWHM for the major elements of REXIS interest (based on requirements) are given in Table 9 below.

Table 9: Detector line widths for elements of interest to REXIS based on requirements

Element	$K\alpha$ Line keV	Full Width at Half Maximum	
		Percent	keV Range
Ni	7.478(15)		
Co	6.930(32)		
Fe	6.403(84)	0.13	6.00 – 6.84
Mn	5.898(75)		
Cr	5.414(72)		
Ti	4.510(84)	0.16	4.156 – 4.88
Ca	3.691(68)	0.18	3.37 – 4.03
K	3.313(94)		
S	2.307(84)		
P	2.013(68)		
Si	1.739(98)	0.26	1.51 – 1.97
Al	1.486(70)	0.29	1.27 – 1.71
Mg	1.253(60)	0.31	1.05 – 1.45
Na	1.040(98)		
O	0.524(90)		

(Lawrence Berkeley National Laboratory Center for X-ray Optics and Advanced Light Source, 2009)

3.3.2. Spectral Resolution Limits

The spectral resolution model, developed jointly by Hong (2012) (in IDL) and Inamdar (2013) (in MATLAB) (Model code files produced in MATLAB (Inamdar, 2013) available in Appendix C.), generates a more accurate looking spectrum with Gaussian-like peaks, unlike the ideal chondrite spectrum (Figure 14). These peaks are then broadened in the model and these broadened cases are

overlaid on the image to show where the model 'breaks' and neighboring peaks are no longer discretely discernible.

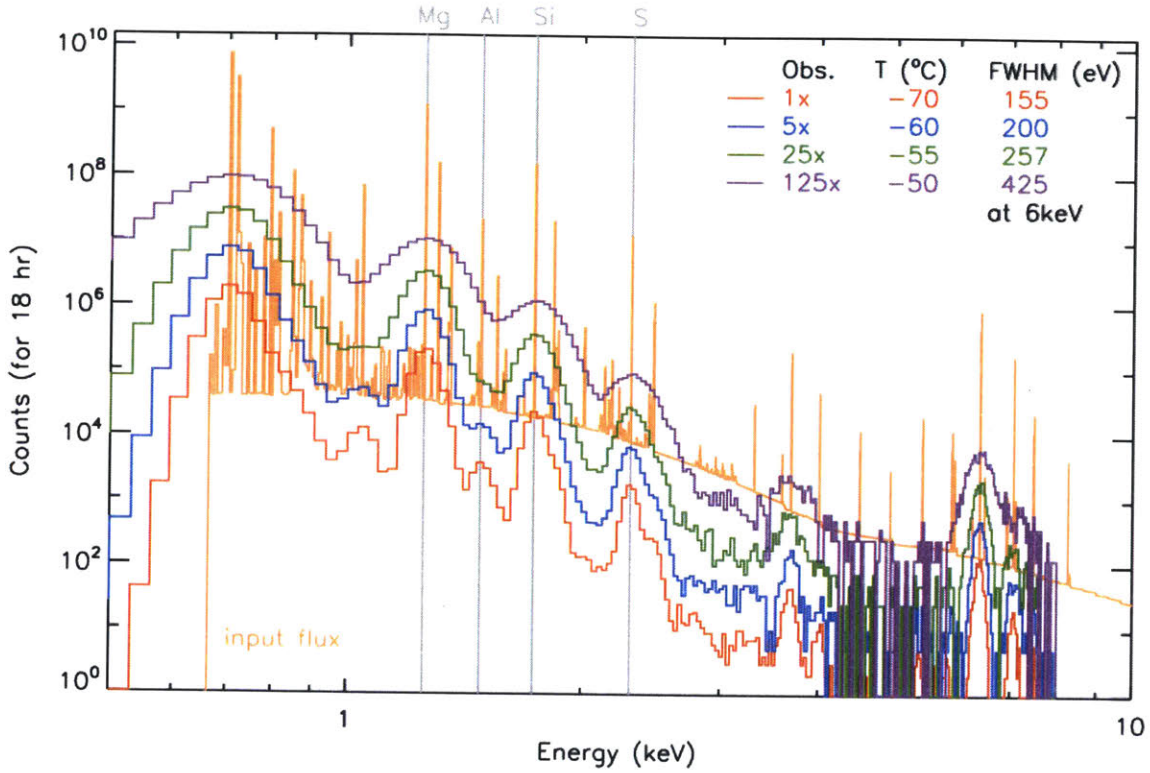

Figure 16: Graphical results of the spectral resolution model in which individual peaks are broadened until the model 'breaks' and elemental lines of interest are no longer discernible. Marked on the graphic are the XRF lines for Mg, Al, Si and S. By following the line broadening results as a function of detector Temperature in °C, we can see that as the CCD detector temperature increases, so does the FWHM in eV of each elemental line. At -70°C these four elemental peaks are all discrete, including Aluminum with the weakest relative intensity within its FWHM. At -60°C Aluminum becomes almost completely buried within the contamination from neighboring lines Mg and Si. By -55°C Aluminum is entirely buried and all lines' FWHM has broadened by approximately 40%. At -50°C all four elemental peaks have broadened substantially by approximately 64%. These results do not include contributions from background radiation (the degrading orange line) and is a subject of ongoing work (Hong, 2012; Inamdar, 2013).

Figure 16 shows the graphical results of the spectral resolution model by broadening the peaks (as a function of increased CCD detector temperature) until the model result 'breaks' and the accuracy requirement is no longer met. Degradation of the lines was commensurate to the detector state per the analytical model for CCD response. At a cool -70°C detector temperature Aluminum can be discerned. The plot shows incremental increase in detector temperature up to -50°C by which point the peaks' FWHM have all broadened by approximately 64%. Being that the detection of Aluminum is not a science requirement of REXIS but rather a science aim, we can see that temperature up to -55°C would be sufficient to meet REXIS requirement REX-3.1.1.

3.3.3. Line Measurement Accuracy Limit

By combining the results of the student experiment on the CCID-41's line detection accuracy (Megyery, REXIS Science Team, 2012) with the equations developed for FWHM as a function of detector temperature and line energy (Sternberg, 2012), we are able to plot the line measurement accuracy of elemental abundance ratios as a function of detector temperature. The results of this combination from the spectral resolution model are shown in Figure 17 below.

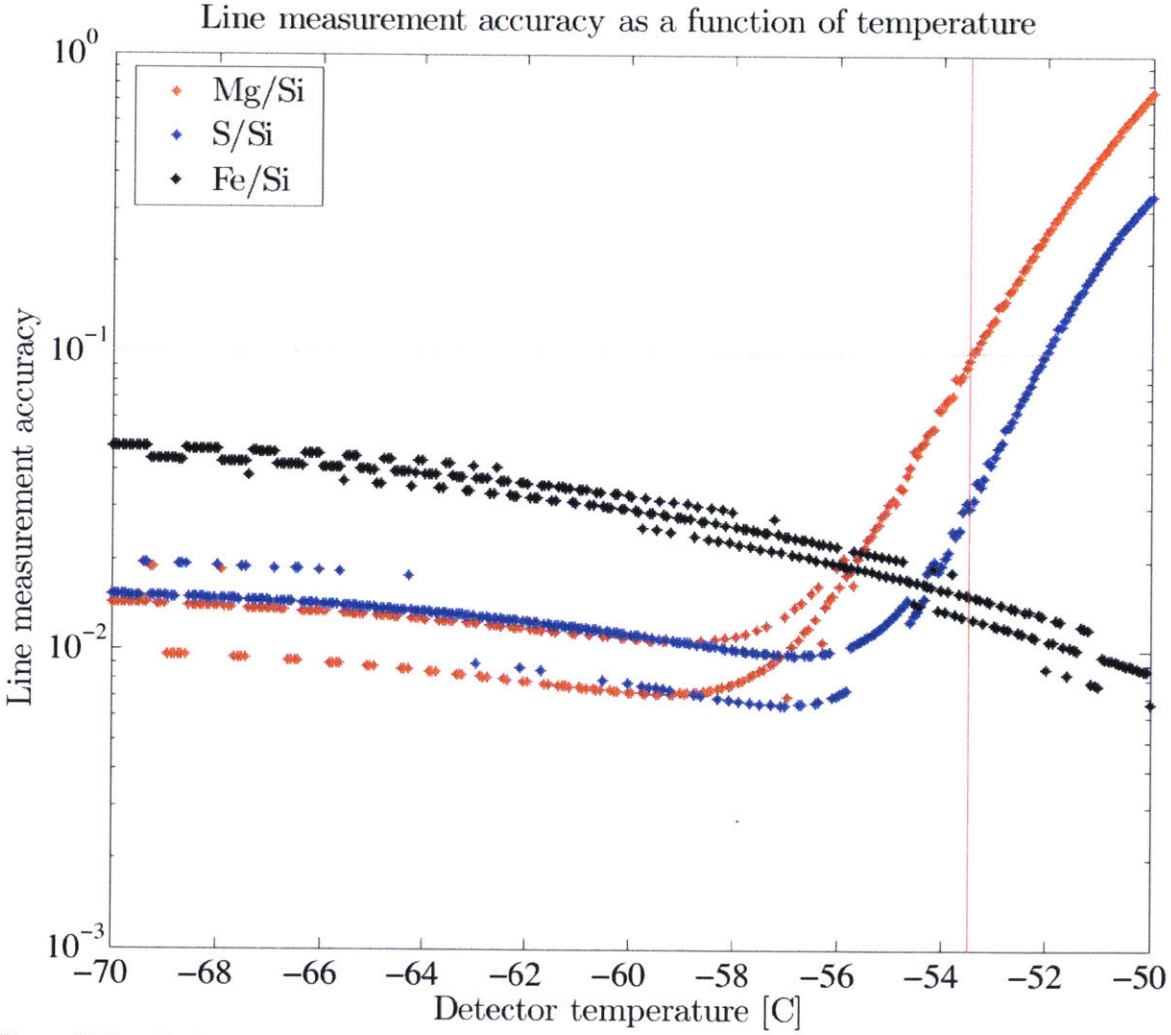

Figure 17: Graphical representation of the line measurement accuracy of elemental abundance ratios as a function of CCD detector temperature. Elemental abundance ratios (Mg/Si, S/Si, Fe/Si) are plotted for their accuracy of the line ratio measurement as a function of detector temperature in °C. The pink horizontal line represents the 10% accuracy requirement set forth by REXIS requirement REX-2.1.1. The intersection of the 10% accuracy requirement with the Mg/Si ratio is the point at which that detection limit of that ratio would surpass the requirement and no longer be discernible. This corresponds to the red vertical line at just above -54°C. Thus, a detector temperature requirement of -55°C would suffice to fulfill REXIS requirement REX-2.1.1 (Image Credit: Inamdar, 2013).

Figure 17 graphically depicts the line measurement accuracy of elemental abundance ratios (Mg/Si, S/Si, Fe/Si) as a function of CCD detector temperature. The REXIS line measurement accuracy requirement of 10% is marked with the horizontal magenta line at $\sim 10^{-1}$ on the vertical axis. The intersection of that line with the Mg/Si ratio is marked by the vertical red line just above -54°C on the horizontal axis. At temperatures warmer than this intersection not only is the accuracy requirement REX-2.1.1 surpassed but these elemental abundance ratios would be discernible due to the FWHM line broadening effects as depicted in Figure 16.

3.4. Results and Recommendations

The results of the spectral resolution model are two-fold and both results indicate a nearly exact maximum threshold for CCD detector temperature in order to remain within REXIS requirements.

In Figure 16 we graphically see the broadening of several elemental line emissions peaks until the model 'breaks' and the elemental lines of interest are no longer discernible. At -55°C the peak for Aluminum is entirely buried within the broadening of neighboring lines Mg and Si. At temperatures beyond -55°C all four elemental lines have broadened substantially by approximately 64% and these results do not include contributions from background radiation. The line-broadening spectral model indicates that the CCD detector should remain at a constant temperature below -55°C in order to remain within the FWHM spectral resolution requirement for REXIS, REX-3.1.1, and be able to obtain useful scientific spectral data.

In Figure 17 we graphically see the representation of the line measurement accuracy of elemental abundance ratios as a function of CCD detector temperature. Elemental abundance ratios (Mg/Si, S/Si, Fe/Si) are plotted for the accuracy of their measurement as a function of detector temperature in °C. The main result of this graphic indicates that the 10% line measurement accuracy requirement is surpassed if the CCD detector temperature exceeds -55°C. At temperatures warmer than this that ratio would surpass the REXIS science requirement REX-2.1.1 and no longer be discernible.

The results of the student experiment (Megyery, REXIS Science Team ETU-1: CCID-41 Laboratory Experimentation, 2012) when combined with the equations for total intrinsic detector noise (Sternberg, 2012) graphically indicate in Figure 11 that total noise versus temperature remains steady until approximately -75°C. Above -75°C the total noise greatly, although linearly and steadily, increases with detector temperature. This graphic result indicates that it is recommended, in order to minimize intrinsic detector noise, that the CCDs onboard the REXIS instrument be held at or below ~-75°C.

The combination of these three results leads to the author's recommendation that a detector temperature requirement be set that the temperature of the CCD detector onboard REXIS shall not exceed -55°C in order to remain within the constraints of the established REXIS Science requirements REX-2.1.1 and REX-3.1.1.

Further, it is the author's recommendation that a detector temperature goal be set that the temperature of the CCD detector onboard REXIS shall not exceed -75°C in order to minimize noise contamination that is intrinsic to the CCID-41 detector that has been chosen for the REXIS instrument.

3.5. Research Needs and Future Work

Spectral resolution modeling determined and verified the detector temperature requirement and recommendation for temperature as dictated by the REXIS spectral resolution requirement REX-3.1.1 and the accuracy of line ratio measurements requirement (accuracy requirement of 10%) REX-2.1.1. The spectral modeling also quantified the spectral contamination of each X-ray fluorescent line into its neighboring lines. The results of the spectral modeling will be used to provide an estimate for photon counts of each X-ray fluorescent line, which can be used for input of imaging and collimation simulation and analysis.

Further, as mentioned with Figure 16 above, those results do not include contributions from background radiation (the degrading orange line) and is a subject of ongoing work. The basis for developing those models can be found in the following subsections regarding instrument background and minimum detectable flux, Section 3.5.1, and instrument background scattering, Section 3.5.2.

3.5.1. Instrument Background Levels and Minimum Detectable Flux

The collecting power of an X-ray Spectrometer can be described in terms of the product of effective area and FOV – which in astronomy is known as Grasp, $G(E)$ (units of $cm^2 sr$) – derived below, for a telescope. Where X-rays in the energy interval $E, E + dE$ are emitted from an extended source (i.e. the surface of 1999 RQ36) and are incident on the instrument aperture with a flux $I(E)$ (in $phot\square ns\ cm^{-2}s^{-1}sr^{-1}keV^{-1}$) then the number of detected photons C detected in time t is given by:

$$C = I(E)G(E)t\ dE$$

The sensitivity of a photon-detecting instrument can be quantified by the minimum detectable flux I_{min}, which is the minimum signal flux from a source that can be distinguished from the background B. Fraser et al. [18] assume than an isotropic flux I (in units of $photons\ cm^{-2}s^{-1}sr^{1}$) of fluorescent X-rays at a discrete energy (in keV) from an extended source is incident on the front of an instrument with a grasp G. The instrument has a focal plane detector with an area for photon detection A_{det} and energy resolution δE. The detected fluorescent X-ray signal is accompanied by a background of solar X-rays which are scattered from the surface under examination, denoted by I_{scat} (in units of $photons\ cm^{-2}s^{-1}sr^{-1}keV^{-1}$).

Although features in the scattered continuum may contain information on surface properties and absorption features in the continuum may yield compositional information, in terms of measure fluorescence spectra the continuum constitutes a background. The detector also has a non-X-ray background component, caused by charged particle events B_p (units of $events\ cm^{-2}s^{-1}keV^{-1}$). For a cooled, photon-counting detector, intrinsic thermal noise is negligible and the scattered X-ray component and the particle-induced background will dominate. If a signal-to-noise ratio R is required for the detection of an X-ray line, then I_{min} may be defined as the flux that, in a given

integration time, produced a count R standard deviations of B above its mean. I_{min} for a given value of R is given by:

$$I_{min} = \frac{R\sqrt{\delta E\left(B_p A_{det} + I_{scat} G\right)}}{G\sqrt{t}}$$

The particle-induced X-ray background B_p results from a combination of both high-energy cosmic rays and lower energy (10-100MeV) protons ejected from the Sun. To reduce B_p REXIS's detectors will be shielded.

3.5.2. Instrument Background Scattering

The following equations show the relationship used to model coherent, I_R, and incoherent, I_C, scatter (J. Hubbell, 1975; D. Cromer, 1965) which constitutes instrument background, or noise. Coherent scatter refers to the condition when the wavelength of the radiated photon energy is equal to that of the incident photon energy. Incoherent scatter refers to the condition when the wavelength of the radiated or scattered photon energy is not equal to that of the incident photon.

The following equation is used to determine coherent scatter at a particular wavelength (Hubbell, 1969). Total coherent scatter associated with a particular energy, E', is determined by doing a double integration across a range of energies which represent the full width at half maximum for that energy, as determined by the energy resolution shown in Table 6. The Gaussian detector response function (R. Hoover, 1972) $P(E, E')$, of the instrument is considered in that integration. Then integration is done again to sum the contributions made at each energy, E.

$$\sigma_R(\lambda) = 0.0239(cos^2\theta + 1)\frac{d\theta}{4\pi}\frac{1}{D}J(\lambda)\cos(\alpha)\frac{\Sigma_i^N\left[(\frac{C_i}{W_i})f_i^2\right]}{\Sigma_i^N\left[\mu_i(\lambda)(1+\frac{\cos\alpha}{\cos\beta}\right]}$$

$$I_R = \int_{E_{min}}^{E_{max}}\int_{E_{min}}^{E_{max}} \sigma_R(E, E', \theta)\, P(E, E')\, dEdE'$$

The following equations are used to determine incoherent scatter at a particular wavelength (Hubbell, 1969) and to determine the integrated incoherent scatter, analogous to the above equation for coherent scatter.

$$\sigma_C(\lambda) = 0.0239\frac{d\theta}{4\pi}A(\lambda_C)\,J(\lambda_C)\cos(\alpha)\frac{\Sigma_i^N\left[\frac{C_i}{W_i}S_i\right]}{\Sigma_i^N\left[\mu_i(\lambda)+\mu_i(\lambda_C)\frac{\cos\alpha}{\cos\beta}\right]}$$

$$I_C = \int_{E_{min}}^{E_{max}} \int_{E_{min}}^{E_{max}} \sigma_C(E, E', \theta)\, P(E, E')\, dE dE'$$

Finally, A, k, and λ_C are defined below:

$$A(\lambda) = \left(1 + k(1 - \cos\theta)\right)^{-2} \frac{1 + cos^2\theta + k^2(1 - \cos\theta)^2}{1 + k(\cos\theta)}$$

$$k = \left[511\left(\frac{\lambda}{12.4}\right) - (1 + \cos\theta)\right]^{-1}$$

$$\lambda_C = \lambda - \left(\frac{12.4}{511}\right)(1 - \cos\theta)$$

The following equation gives the Gaussian response of the detector (R. Hoover, 1972).

$$P(E, E') = \frac{exp - \left[\frac{(E - E')}{2\sigma_m^2 E'}\right]}{\sigma_m (2\pi E')^{0.5}}$$

Table 10 defines additional parameters used in calculating scatter (P. Clark J. T., 1997; Clark, 1979; Hubbell, 1969).

Table 10: Additional terms used in the above equations to model scatter from the surface

Term	Definition	Description
θ	Backscatter Angle	Incident plus exiting flux angle
A	Angular distribution function	Equation defined above
W_i	Atomic weight for each element	Given for each element
S_i	Incoherent scattering factor for i elements	Spline fit to NBS table, q dependent
f_i	Coherent scattering factor for i elements	Spline fit to NBS table, q dependent
q	$\frac{\sin(\theta/2)}{\lambda}$	Calculated at each wavelength
$P(E, E')$	Shape of detector response at each energy	Resolution-dependent Gaussian

(Hubbell, 1969)

Source flux and energy absorption need to be considered, just as in fluorescence line production calculations. In addition, the backscatter angle, θ, is significant because only X-rays which are deflected back from the surface at the proper angle will be able to enter the detector. At the sub-solar point (the Sun is directly overhead), that angle is $180°$ (relative to the incident solar flux angle). The constant 0.0239 is the product of the multiplication of Avogadro's number by half of the square of the electron radius. This constant puts the scatter intensity on a molar rather than an atomic basis. A spline fit was done to published tables of coherent and incoherent scattering factors, f_i and S_i respectively, which vary as a function of the parameter q (J. Hubbell, 1975; D. Cromer, 1965). Additional parameters need to be considered in the case of incoherent scatter: the wavelength of the incident flux, λ_C, called the Compton wavelength, is shorter than the wavelength of the resulting scattered flux, λ_i.

Bibliography

A. Milani, S. R. (2009). Long Term Impact Risk for (101955) 1999 RQ36. *Icarus, 203*(2), 460-471.

A. W. Harris, J. S. (2002). Asteroids in the Thermal Infrared. *Asteroids III*, 205-218.

Allen, B. (2012). Solar Flux Incident on the Asteroid for Various Flare States. Cambridge, MA, USA.

Aschwanden, M. J. (2006). *Physics of the Solar Corona* (2 ed.). Springer.

Bautz, M. (2004). Progress in X-ray CCD Sensor Performance for the Astro-E2 X-ray Imaging Spectrometer. *SPIE, 5501*(1), 111-122.

Binzel, R. P. (2011, 10). MIT Course 12.410 Astronomy Laboratory Techniques Lecture.

Bouwer, D. (1983). Intermediate-Term Epochs in Solar Soft X-ray Emission. *J. Geophysical Research, 88*, 7823-7830.

C. E. Schlemm, R. D. (2007). The X-ray Spectrometer On the MESSENGER Spacecraft. *Space Sci. Rev., 131*, 393-415.

Clark, P. (1979). *Comparison on theoretically calculated and observed XRF data, in Correction, correlation, and Theoretical Consideration of Lunar X-ray Fluorescence Intensity Ratios.* University of Maryland, College Park.

D. Cromer, J. W. (1965). Scattering Factors From Relativistic Dirac-Slater Wave Functions. *Acta Crystallogr, 18*, 104-109.

D. S. Lauretta, B. K. (2001). Thermal Analysis of Labile Trace Elements in CM and CV Carbonaceous Chondrites Using Inductively Coupled Plasma-Mass Spectrometry. *Lunar and Planetary Institute Science Conference Abstracts, 32*, p. 1356.

Donnelly, R. (1976). Empirical Models of Solar Flare X-ray and EUV Emission For Use In Studying Their E and F Region Effects. *Journal of Geophysical Research, 81*, 4745-4753.

G. W. Fraser, J. D. (2010). The Mercury Imaging X-ray Spectrometer (MIXS) on BepiColombo. *Planetary and Space Science, 58*, 79-95.

Goldsten, J. O. (1998). The NEAR X-ray/Gamma-Ray Spectrometer. *Johns Hopkins APL Technical Digest, 19*(2), 126-135.

Grieken, G. (2002). *Handbook of X-ray Spectrometry* (Second Ed ed.). (A. Markowicz, Ed.) New York: Marcel Dekker, Inc.

H. Campins, A. M. (2010). The Origin of Asteroid 101955 (1999 RQ36). *The Astrophysical Journal Letters, 721*(1), L53.

H. Campins, K. H.-A.-D. (2010). Water Ice and Organics On the Surface of the Asteroid 24 Themis. *Nature, 464*(7293), 1320-1321.

Hamamatsu Photonics K.K. (n.d.). *EM-CCD Technical Note.* Retrieved 03 12, 2012, from http://www.graftek.com/pdf/AppNotes/hamamatsu/EMCCDTECHnote.pdf

Hapke, B. (2001). Space Weathering From Mercury To the Asteroid Belt. *Journal of Geophysical Research, 106.E5*, 10039-10.

Harris, A. (1998). A Thermal Model For Near-Earth Asteroids. *Icarus, 131.2*, 291-301.

Hong, J. S. (2012). Spectral Line Broadening. Cambridge, MA.

Howell, S. B. (2000). *Handbook of CCD Astronomy.* Cambridge: Cambridge University Press.

Hubbell, J. (1969). *Photon Cross-Sections, Attenuation Coefficients, and Energy Absorption Coefficients from 10keV to 100geV.* Washington, D.C.: Natl. Bur. Stand.

I. Adler, J. G. (1972). The Apollo 15 X-ray fluorescence experiment. *Proc. Lunar Science Conference, 3*, pp. 2157-2178.

I. Adler, J. T. (1970). *Geochemical Exploration of the Moon and Planets.* New York: Springer-Verlag.

I. J. Adler, J. T. (1977). Orbital chemistry: lunar surface analysis from X-ray and gamma-ray remote sensing experiments. *Phys. Chem. Earth, 10*, 17-43.

Inamdar, N. (2013). FWHM as a Function of Temperature: Experimental Data Result.

J. Hubbell, W. B. (1975). Atomic Form Factors, Incoherent Scattering Functions, and Photon Scattering Cross-Sections. *J. Phys. Chem. Ref. Data, 4*, 471-537.

J. Naranen, H. P. (2007). X-ray Fluorescence Modeling for Solar System Regoliths: Effects of Viewing Geometry, Particle Size, and Surface Roughness. In D. V. G. B. Valsecchi (Ed.), *Proceedings of the 236th IAU Symposium* (pp. 43-250). Cambridge University Press.

J. Naranen, H. P. (2008). Laboratory Studies Into the Effect of Regolith on Planetary X-ray Fluorescence Spectroscopy. *Icarus 198*, pp. 408-419.

J. R. Spencer, L. A. (1989). Systematic Biases In Radiometric Diameter Determinations. *Icarus, 78.2*, 337-354.

J. W. Criss, L. S. (1968). Calculation Methods for Fluorescent X-ray Spectrometry: Empirical Coefficients Versus Fundamental Parameters. *Anal. Chem., 40*, 1080-1086.

Jagoutz, O. (2011, 02). Simple Geochemical Modeling to Understand the Planetary Accretion Processes and Core Formation. Cambridge, MA, USA: MIT.

Janesick, J. (2001). *Scientific Charged-Coupled Devices.* Bellingham: SPIE Press.

K. Koyama, e. a. (2006). X-ray Imaging Spectrometers (XIS) on Board Suzaku. *PASJ: Publ. Astron. Soc. Japan.*

L. R. Nittler, R. D. (2001). X-ray Fluorescence Measurements of the Surface Elemental Composition of Asteroid 433 Eros. *Meteorites Planet Sci., 36*, 1673-1695.

L. Yin, J. T. (1993). Remote X-ray spectrometry. *Remote Geochemical Analysis: Elemental and Mineralogical Composition*, pp. 199-202.

Lawrence Berkeley National Laboratory Center for X-ray Optics and Advanced Light Source. (2009). *X-ray Data Booklet.* Retrieved 12 07, 2011, from X-ray Data Booklet: http://xdb.lbl.gov

Lim, L. F. (2005). *Asteroid Spectroscopy: I. A Thermal Infrared Survey of Asteroids II. X-ray Fluorescence Spectroscopy of 433 Eros.* PhD Dissertation, Cornell University.

Lucy Lim, N. G. (2012). X-ray counts as a function of energy for various solar states.

M. Delbo, P. M. (2011). Temperature History and Dynamical Evolution of (101955) 1999 RQ36: A Potential Target For Sample Return From a Primitive Asteroid. *The Astrophysical Journal Letters, 728.2*, L42.

M. Mueller, M. D. (2011). ExploreNEOs. III. Physical Characterization of 65 Potential Spacecraft Target Asteroids. *The Astronomical Journal, 141.4*, 109.

Megyery, S. (2012). REXIS Science Team ETU-1: CCID-41 Laboratory Experimentation. Cambridge, MA.

Megyery, S. (2013, 01 15). Counts as a function of energy. Cambridge, MA.

MIT/Harvard Aperture & Detector Team. (2011).

MIT/Harvard REXIS Structures Team. (2011).

MIT/Harvard REXIS Team. (2013).

N. Crosby, M. A. (1993). Frequency Distribution and Correlations of Solar X-ray Flare Parameters. *Solar Physics, 143*, 275-299.

National Geophysical Data Center. (1991). *Solar-Geophysical Data Comprehensive Reports.* Boulder, CO: National Geophysical Data Center.

P. Clark, B. R. (1990). The relationship between orbital, Earth-based, and sample data for lunar landing sites. *Proc. Lunar Planetary Science Conference 20th*, (pp. 147-160).

P. Clark, I. A. (1978). Utilization of independent solar flux measurements to eliminate nongeochemical variation in X-ray fluorescence data. *Proc. Lunar Planetary Science Conference 9th, 3*, pp. 3029-3036.

P. Clark, J. T. (1997). Remote X-ray Fluorescence experiments for future missions to Mercury. *Planetary Space Science*(45), 57-65.

Pryor, C. (n.d.). *CCD Characteristics.* Retrieved 03 12, 2012, from http://www.physics.rutgers.edu/~pryor/ph629/lab2.pdf

R. Donnelly, D. B. (1981). SMS-GOES Solar Soft X-ray Measurements, Parts I and II. *NOAA Tech. Memo, ERL*(SEL-56 and SEL-57).

R. Hoover, R. T. (1972). Advances in Solar and Cosmic X-ray Astronomy: A Survey of Experimental Techniques and Observational Results. *Adv. Space Sci. Technol., I*, 1-214.

R. Jenkins, J. D. (1967). *Practical X-ray Spectrometry.* New York: Springer-Verlag.

R. Kreplin, K. D. (1977). The Solar Spectrum Below 10A. In K. D. R. Kreplin, *Solar Output and its Variation* (pp. 287-312). Boulder, Colorado: Associated University Press.

R. Michelson, A. N. (2006). Spectroscopy of near-Earth asteroids. *Astronomy & Astrophysics, 451*, 331-337.

S. Sasaki, K. N. (2001). Production of Iron Nanoparticles by Laser Irradiation In a Simulation of Lunar-Like Space Weathering. *Nature, 410.6828*, 555-557.

Sephton, M. A. (2002). Organic Compounds In Carbonaceous Meteorites. *Natural Products Reports, 19.3*, 292-311.

Sternberg, D. C. (2012). *REXIS Spectral Resolution as Determined by Operating Temperature.*

T. Okada, e. a. (2006). X-ray Fluorescence Spectroscopy of Asteroid Itokawa by Hayabusa. *Science, 312*(5778), 1338-1341.

T. Okada, K. S. (2006). X-ray Fluorescence Experiments of Asteroid Itokawa by the XRS Onboard Hayabusa. *Lunar and Planetary Science, XXXVII.*

T. Okada, K. S. (2006). X-ray Fluorescence Spectrometry of Asteroid Itokawa by Hayabusa. *Science, 312*, 1338-1341.

T. Okada, K. S. (2007). Elemental Composition of Asteroid Itokawa by Hayabusa XRF Spectrometry. *Lunar and Planetary Science, XXXVIII.*

T. Okada, M. K. (2000). X-ray Fluorescence Spectrometer Onboard Muses-C. *Adv. Space Res., 25*(2), 345-348.

T. Okada, M. K. (2002). Elemental Mapping of Asteroid 1989ML From MUSES-C Orbiter. *Adv. Space Res., 29*(8), 1237-1242.

T. Okada, T. A. (2005). First X-ray observation of lunar farside from Hayabusa X-ray spectrometer. *Lunar and Planetary Science, XXXVI.*

Taylor, S. (1975). Lunar Science: A Post-Apollo View.

The University of Arizona, NASA Goddard Space Flight Center. (2013, 01 08). *OSIRIS-REx Asteroid Sample Return Mission.* Retrieved 01 15, 2013, from Mission Objectives: osiris-rex.lpl.arizona.edu/?q=objectives/objectives_background

The University of Arizona, NASA Goddard Space Flight Center. (2013, 01 08). *OSIRIS-REx Asteroid Sample Return Mission.* Retrieved 01 15, 2013, from Science Objectives: osiris-rex.lpl.arizona.edu/?q=objectives/science_objectives

Y. Maruyama, K. O. (2008). Laboratory Measurements of Particle Size Effect in X-ray Fluorescence and Implications to Remote X-ray Spectrometry of Lunar Regolith Surface. *Earth Planets Space, 60*, 293-297.

Zombeck, H. (1990). The Solar Spectrum. In H. Zombeck, *Handbook of Space Astronomy and Astrophysics.* New York: Cambridge University Press.

Appendix A: Context of Student Work

This work is a continuation of research begun during the 2011-2012 academic year. The MIT Aeronautics & Astronautics Department's year-long capstone project course(s) known as (16.831/12.431) Space Systems Engineering and (16.832/12.432) Space Systems Development was a group of approximately 20 senior-level students introduced to the REXIS Instrument project.

During the first semester, Fall 2011, a great deal of background research and study was conducted by all students to understand the level of science and engineering needed to make a real contribution to the design and development of the instrument. In the Spring of 2012 a goal was set to build the first Engineering Test Unit (ETU-1) of the REXIS Instrument with the goal of the REXIS ETU-1 to detect X-rays from two point sources and a continuous source and read out that data to produce the respective elemental lines on a histogram.

The author was the only student registered for the course from the MIT EAPS Department and thus took on the role as the Science Team Lead. She even served as student representative at the All-Instruments Team Meeting in Tucson, Arizona in November 2011 to introduce the class's progress on the Instrument at the OSIRIS-REx headquarters at the University of Arizona.

As of the Fall of 2012 the REXIS Instrument design and development had become too advanced to introduce to a new group of students and the project has remained in the hands of the faculty, researchers, staff and graduate students still involved. Fall 2012 served as the author's final semester of her MIT undergraduate career and she opted to remain on the team as a contributor to the development and analysis of REXIS science. Thus, the logical progression of the science work on REXIS was to complete her undergraduate thesis requirement for partial fulfillment of the Degree of Bachelor of Science in the Department of Earth, Atmospheric and Planetary Sciences at MIT.

Appendix B: Supplemental Reading

B.1. REXIS Heritage of CCDs for XRF Detection

Remote sensing of X-ray emissions is only possible for bodies with little or no atmosphere to absorb these emissions (Goldsten, 1998). Orbital, rather than flyby, missions are preferred for such measurements because of the typically long observation times required. The REXIS CCD-based spectrometer is built on flight heritage that needs to be examined in detail. This examination will discuss what XRF is in the context of past missions, how they were developed, the more detailed theory behind the mechanism by which each worked, and to outline, with each case study example, the various applications of XRF.

Particularly, each case study has not been without its own set of challenges, some of which the respective science teams were capable of overcoming. Thoroughly understanding the scientific flight heritage of the REXIS Instrument design and science trades can lead to a comprehensive understanding of the X-ray spectroscopy of asteroids and aid in the understanding of the X-ray spectroscopy of REXIS at 1999 RQ36.

B.1.1. Hayabusa

X-ray fluorescence spectrometry of asteroid 25143 Itokawa was performed by the X-ray spectrometer onboard Hayabusa during the first touchdown on 19 November 2005. The mission's intent was to determine major elemental composition of the asteroid surface and its regional variation by observing the X-rays excited by solar X-ray irradiation by the X-Ray Spectrometer (XRS) on board. Further, they hoped that information on surface roughness would be derived from observations at various phase angles.

B.1.1.1. XRS Instrumentation and Observation

The XRS was an advanced XRF spectrometer with a light-weight (1.5 kg) sensor unit based on a CCD X-ray detector; this was the first time a CCD had been use for such a purpose on a planetary mission (T. Okada e. a., 2006). A CCD was chosen for use as an X-ray detector to improve energy resolution and to extend detection energy range (T. Okada M. K., 2000). Four CCD chips were arrayed to detect X-rays from the asteroid. Another single chip was obliquely mounted to detect X-rays from the standard sample plate that solar X-rays would excite (T. Okada M. K., 2002).

The Standard Sample Plate (SSP) was for concurrently calibrating the XRF when it was excited by the Sun. The SSP was a glassy plate whose composition was intermediate between those of chondrites and basalts. By comparing X-ray spectra from the asteroid and from the SSP, quantitative elemental analysis could be achieved, although the intensities and spectral profiles of solar X-rays change over time (T. Okada e. a., 2006).

The XRS instrument was required to have (1) energy resolution sufficient to discriminate fluorescent X-rays of major element and reject scattered solar X-rays as backgrounds, (2) energy detection range

from 0.7 to 8 keV, (3) effective detection area to accumulate statistically significant counts of X-ray photons in a given integration time and (4) concurrent solar X-ray monitoring for quantitative elemental analysis (T. Okada M. K., 2002). There were also several technical constraints on small mass budget, mechanical and thermal conditions that the orbiter undergo during the mission, and mounted position in the Hayabusa orbiter.

The CCD-based XRS consisted of a detection system (XRS-S) and an electronic circuit (XRS-E). The specifications of the instrument are shown in Figure 1 below. To achieve the smaller size and larger active area, a full-frame transfer method was adopted as the CCD readout, where no inactive transfer regions or data storage areas were demanded. The active area of each chip was 1 inch square with 1024 x 1024 pixels. Each pixel size was 24 micro-m square. To attain high-energy resolution, the CCD chips were operated below 230K to reduce the thermal noise level. The hood was effectively designed for the Radiative cooling. To extend the lower limit of the detection energy range, the windows with 5 micro-m thick beryllium films supported by meshed grids and latticed frames of 90% transparency were used to shield the visible light as well as effectively pass the X-ray photons below 1 keV. The signal readout took place every 8 micro-sec in turn by multiplexing the five chips. 16 pixels in a line were binned as a single data to readout in 0.5 sec per chip.

Table 11: Specifications of the XRS Instrument onboard Hayabusa

Specifications of the XRS	
Total Mass	3.3 +/- 0.3 kg
Total Power	12 +/- 3 W
Detectors	1"CCD x 4 chips (main) x 1 chip (solar monitor)
Energy Range	0.7 – 10 keV
Energy Resolution	90 eV at Al-K
Field of View	3 deg (main)
Detection Area	25 cm^2 (main)
Count Rate	A few to 100 cps dependent on solar activity
Operation Temperature	< 230 K
Readout Rate	125 kHz line-binning of 16 pixels
ADC	12 bit
Time Resolution	600 sec
Observation Mode	Normal 0.2 kbps / Calibration Mode

(T. Okada M. K., 2000)

The electronic circuit was composed of the CCD driver, multiplexer, data handling circuit, thermo-electric cooler driver, CUP and interface for command and telemetry, and power supply. The clock patterns from the driver were multiplexed and delivered to five CCD chips in turn. The readout signals from each chip were received into the data handling circuit and, after digitized by a 14-bit ADC, the upper 12 bits were stored in the FIFO. If the signals were beyond a threshold level, they were regarded as X-ray events. After a given integration time of 60 sec, they were formatted as CCSDS packets and transmitted to the data-handling system of the spacecraft (T. Okada M. K., 2000). The data handling was controlled by using the specified 32-bit Hitachi SH-3 CPU.

In-flight performance of the XRS was confirmed by observations of X-rays from the SSP, X-ray-emitting bodies such as Kepler's supernova remnants, and X-rays from the far side of the Moon.

In-flight calibration was performed by observation of cosmic X-rays along the trajectory of the orbiter. In situ calibration of X-ray fluorescence by solar X-ray irradiation into the onboard standard sample was used to improve the accuracy of the quantitative elemental analysis (T. Okada M. K., 2000).

During the descent, the solar phase angle – the angle between the Sun, Itokawa, and Hayabusa – was between 5° and 10°. This small phase angle is favorable for performing XRF spectrometry (T. Okada e. a., 2006). At larger phase angles, shadows on the rough surface terrain can interfere with the elemental analysis (T. Okada e. a., 2006). During descent, the XRS continued X-ray spectrometry of Itokawa, and the SSP simultaneously excited by the Sun, so that the entire asteroid surface was observed in a longitudinal direction due to its rotation.

The effective field of view of the XRS was 3.5° by 3.5°, corresponding to a "footprint" size of 87 m by 87 m at an altitude of 1.4 km, which became proportionally smaller as Hayabusa descended. Consequently, the XRS observed local areas of Itokawa 550 m by 298 m by 244 m in size. XRS observations were sometimes affected by background radiation from space (X-rays and energetic particles) because the footprint was not centered on the asteroid, due to the rotation of the irregularly shaped asteroid and instability of the spacecraft's attitude control that resulted from the failure of two of the three reaction wheels.

B.1.1.2. X-Ray Spectrometer Data and Analysis

The XRS produced a set of X-ray energy spectra of Itokawa and the SSP, after onboard processing of data from each CCD, every 5 min. Much of the data could not be analyzed due to unfavorable solar activity, but six data sets with good signal-to-background ratios – observed during periods of relatively enhanced solar activity – were selected.

The descent phase data was the most desirable condition because of relatively high solar activity for X-ray excitation and low altitude to fill the 3.5 x 3.5 degrees field of view of the XRS by the asteroid surface (T. Okada K. S., 2007).

Quantitative elemental analysis of Mg, Al, and Si, and qualitative analysis of Ca and Fe indicated that the surface of Itokawa has chondritic composition and that LL- or L-chondrites are most likely, but H-chondrites or primitive achondrites cannot be rejected (T. Okada e. a., 2006; T. Okada K. S., 2007; T. Okada K. S., 2006).

B.1.2. Suzaku

Suzaku was Japan's 5th X-ray astronomy satellite, an Earth-orbiting observatory imaging various X-ray sources launched in 2005. Suzaku was equipped with an X-ray Imaging Spectrometer (XIS) system, consisting of state-of-the-art CCDs optimized for X-ray detection, camera bodies and control electronics (K. Koyama, 2006).

B.1.2.1. XIS Instrumentation and Observation

From Koyama et al. (2006), the XIS consisted of four CCDs, each placed at the focus of a dedicated X-ray telescope. The XIS camera body consisted of a hood, bonnet and base. The hood had five baffles to block stray light. The bonnet included a vacuum valve, an optical blocking filter (OBF), calibration sources (^{55}Fe), a pressure sensor, a paraffin actuator and a door. The base contained an X-ray CCD mounted on an alumni (Al_2O_3) substrate and was attached to a heat sink assembly made of copper. A Peltier cooler incorporated in the heat sink could cool the detector to its on-orbit operating temperature of -90°C. Over the frame-store region of the CCD, an aluminum shield with a gold-plated nickel surface treatment was placed to block X-ray irradiation. The surfaces of the substrate, the heat sink assembly and the shield were also plated with gold. The bonnet and the hood were made of Al with black surface finish. The inside of the base was Ni-plated, except for the feed-through plate which was gold electro-plated. Multi-layer insulators to reduce heat-flow from the satellite body covered the XIS sensor.

Each XIS sensor had three ^{55}Fe calibration sources. One was attached to the door, and illuminated the whole imaging area. This calibration source was used on the ground and for initial on-orbit calibration before the door was opened. For normal observation, after the door was opened, this calibration source was out of the field of view of the CCD. The other two calibration sources were located on a side wall of the bonnet and illuminated the two far-end corners of the imaging area.

The XIS had four sensors and each sensor had one CCD chip, which was a MOS-type three-phase CCD operated in the frame transfer mode. The imagine area of the CCD had 1024 x 1024 pixels. The pixel size was 24 μ m x 24 μ m, giving a size of 25 mm x 25 mm for the imaging area. These XIS CCD detectors were fabricated in the MIT Lincoln Laboratory and are very similar to the ones flying on the REXIS instrument.

The XIS had a high X-ray spectra range in 0.2 to 12 keV energy band, where the bulk of K-shell lines of O-Ni exist.

B.2. Challenges to XRF: Regolith Effects

The Näränen, et al. (J. Naranen H. P., 2008) study has relevance for the OSIRIS-REx and REXIS mission. REXIS will produce data that shall have well-defined observation angles and also has a large effective area. It can be expected that the regolith effects, if not accounted for, will play a significant role as a source for error in the interpretation of the data from the REXIS mission.

Näränen, et al. (J. Naranen H. P., 2008) presented new measurements and results from their experimental study on how the surface roughness of the regolith affects the interpretation of X-ray spectra obtained by orbiting spacecraft. The surface roughness tends to harden the measured spectrum as the illumination angle increases in a way that the traditionally used FPE of X-ray fluorescence cannot predict.

Fluorescent soft X-rays from the surfaces of atmosphereless planetary bodies in the inner solar system have been measured by instruments on several spacecraft, e.g. Apollo 15 and 16 (I. Adler J. G., 1972), NEAR Shoemaker (L. R. Nittler, 2001), and Hayabusa (T. Okada K. S., 2006). An X-ray

spectrometer is currently travelling to Mercury onboard the MESSENGER spacecraft (C. E. Schlemm, 2007). The soft X-ray energy region is considered to lie between 0.5 and 10 KeV, where fluorescent X-ray emission follows photoionization by incident X-rays and charged particles.

The source of exciting X-rays, in XFS of atmosphere-less bodies, is the solar corona. The Sun is a relatively weak source of X-rays and the fluorescence process is not very efficient and thus studies are limited to the inner solar system, including NEOs such as RQ36.

Traditionally, analysis of X-ray spectra has assumed that surfaces can be considered to be homogeneous and plane-parallel media (P. Clark J. T., 1997). This has been a reasonable approximation considering the relatively poor spectral and spatial resolution of the detectors used for XFS studies to date (J. Naranen H. P., 2008). It has been shown, however, that elemental line intensities and their ratios are affected by the physical properties of the target surface and the viewing and illumination geometry of observations. An increase in line intensities has been measured as particle size in the sample is decreased and a spectral hardening (enhancement of higher-energy end over the lower-energy end) is observed as a function of increasing phase angle (i.e., the angle between the X-ray source and the detector as seen from the sample).

X-ray fluorescence can be analytically calculated by using what is traditionally called the fundamental parameters equation (FPE) of X-ray fluorescence. FPE normally assumes a smooth, flat, and homogeneous surface. As can be seen in the treatment below, the output of the FPE is highly dependent on the spectrum of the incident radiation and the elemental composition of the sample. The FPE derivation here follows that of Grieken and Markowicz (Grieken, 2002). Detailed derivation can also be found in, e.g., Criss and Birks (J. W. Criss, 1968).

For a single element I, the linear photoionization coefficient $\mu_{photo,i}(E)$ and the total extinction coefficient $\mu_{total,i}(E)$ in (1/m) are given by:

$$\mu_{photo,i}(E) = \sigma_{photo,i}(E) f_i \rho$$

$$\mu_{total,i}(E) = \sigma_{total,i}(E) f_i \rho$$

In the equations above $\sigma_{photo,i}(E)$ is the photoionization cross section, $\sigma_{total,i}(E)$ the total extinction cross section, both in [m^2/atom], ρ the total number density of the material in [atom/m^3], and f_i the number density fraction of element i.

Now, the total photoionization and extinction coefficients, ($\mu_{photo,i}(E)$ and $\mu_{total,i}(E)$, respectively) of the material are:

$$\mu_{photo,i}(E) = \sum_i \mu_{photo,i}(E)$$

$$\mu_{total,i}(E) = \sum_i \mu_{total,i}(E)$$

For each photon of energy E absorbed by the element i, the probability of Kl line fluorescence ($l \in \{\alpha, \beta\}$) is:

$$Q_{i,l} = \omega_K f_{i,Kl} \frac{J_{i,K} - l}{J_{i,K}}$$

In the equation above $J_{i,K}$ is the jump ratio of the K shell of the element i, ω_K is the fluorescence yield of the K shell, and $f_{i,Kl}$ is the transition probability.

With the given parameters, we obtain an analytic expression for the first-order Kl fluorescence $F_{i,l,E}(E)$ from element i for incident intensity I_o of a single energy E:

$$F_{i,l,E}(E) = I_o(E) Q_{i,l} \frac{\mu_{photo,i}(E)}{\mu_{total}(E)} \frac{1}{\cos\iota + \mu_{total}(E_l) / \mu_{total}(E)} \cos\epsilon$$

and, finally, for a continuous spectrum we have the total fluorescence intensity $F_{i,l}$ as:

$$F_{i,l} = \int_0^\infty I_0(E) F_{i,l,E}(E) dE$$

Realistic regolith-like surfaces are yet to be analytically modeled for FPE (C. E. Schlemm, 2007). Also, secondary fluorescence (fluorescence excited by fluorescent X-rays) and contributions from elastic and inelastic scattering need to be included in the future, although their contribution to the overall outcome of the calculations is not very significant (C. E. Schlemm, 2007).

Change of spectral shape (and thus relative intensity ratios) is predicted by the FPE to occur as the illumination angle increases. The FPE also describes the apparent discrepancy in the overall behavior of the relative elemental line ratios measured by a downward trend setup versus an upward trend setup as the overall behavior is a function of, e.g., the X-ray source spectrum. However, the FPE does not take into account the physical properties of the sample surface, such as surface roughness, porosity, and particle-size distribution.

For the measurement geometry in the experimental setup conducted by Näränen et al (J. Naranen

H. P., 2008), the most notable effect caused by the physical properties of the regolith is shadowing of the incident X-rays (Y. Maruyama, 2008; J. Naranen H. P., 2008). Qualitatively this means that, as the incident angle increases (large ι), the exciting radiation has an increasing chance of entering the sample medium through the side of a particle, a pore, or a roughness feature. The fluorescent X-rays excited by this radiation have to travel further inside the medium to be observed by a detector looking in the direction of the surface normal than X-rays excited by radiation that entered the medium at a point closer to the detector (i.e., closer to the interface between the regolith and free space). The mean-free path of soft X-rays in a regolith-like medium increase as a function of X-ray energy. Thus fluorescent X-rays of higher energies can escape the medium more freely than those with lower energies. This introduces a hardening of the spectrum as a function of the incidence angle. This effect is described by the equation used in the derivation of the FPE.

Näränen et al. (2008) report that regolith effects are apparent in each line ratio they studied, except for Ti-Kα/Ca-Kα where the energy separation between the two lines is small (i.e., only small effects are to be expected). The qualitative conclusion drawn by Näränen, et al. (2008) from the measurements in their experiment: as the surface roughness increases, the regolith effects increase and cause hardening of the spectrum.

Appendix C: Spectral Resolution Model Computational Methods

C.1. MATLAB Source Code: Updated_Spectral_Res_for_Loop

```
function accuracy = Updated_Spectral_Res_for_Loop(T)


%%%%%%%%%%%%%%%%%%%%%%%%%%%%%%%%%%%%%%%%%%%%%%%%%%%%%%%%%%%%%%%%%%%%%%%%%%%%%%%%
% Updated spectral resolution code
%
%      Niraj Inamdar
%            15 January 2013
%%%%%%%%%%%%%%%%%%%%%%%%%%%%%%%%%%%%%%%%%%%%%%%%%%%%%%%%%%%%%%%%%%%%%%%%%%%%%%%%

% Set baseline line against which you want to measure the ratios
baseline_element = 'Si-K';

% Set the allowable accuracy eta
eta = 0.1;

% Set input temperature in Kelvin
T = T;

% Bring in information regarding spectral lines of interest;
% spectIDs is a structure:
% spectIDs.peakID(i) gives the ith peaklines
% spectIDs.energy(i) gives the energy of the ith peak
% spectIDs.elName(i) gives the identity of the ith peak

spectIDs = spectID_info;

% Import chondrite spectrum; this could be substituted for with the solar
% spectrum; see solarSpectRead for more on how to pull that info out.

C1_data_Ens = importdata('C1_chondrite_spectrum_E.csv');
eV_vals = C1_data_Ens(:,2); % In electronvolts
eV_vals = eV_vals(3:end);
%C1_data_Flux = importdata('C1_chondrite_spectrum_F.csv');
C1_data_Flux = xlsread('C1_chondrite_spectrum_F.csv');
lines = C1_data_Flux(:,2);
bkg = C1_data_Flux(:,3);
total_intensity = lines + bkg;

% Define lines of interest; these must be strings with length between the
% 's of 4
lines_of_interest = ['Mg-K ';'Al-K ';'Si-K ';'S-K ';'K-Ka '];
lines_of_interest = cellstr(lines_of_interest);

% Construct a structure with just the lines we want base on the definitions
% above
lines_to_probe = struct('peakID',[1:length(lines_of_interest)],...
       'energy',zeros(1,length(lines_of_interest)),...
       'intensity',zeros(1,length(lines_of_interest)),'elName',{{}});
for i = 1:length(lines_of_interest);
       for j = 1:length(spectIDs.elName)
              if strcmp(lines_of_interest(i),spectIDs.elName(j)) == 1
                     lines_to_probe.elName(i) = spectIDs.elName(j);
                     lines_to_probe.energy(i) = spectIDs.energy(j);
```

```
                energy_index = indexFind(spectIDs.energy(j),eV_vals);
                lines_to_probe.intensity(i)= total_intensity(energy_index);
            end
        end
end

%figure
semilogy(eV_vals,total_intensity,'b')
hold all

% lines_to_probe now has all the information we need

% Input model for FWHM as a function of energy; this is from Suzaku. The
% linear regression has an input energy in keV; the output of the model is
% in terms of eV
FWHM_en = 11.922*(lines_to_probe.energy/1000) + 52.989;

% Input model for FWHM as a function of temperature; this is from the data
% linefit and the same for each line; we will then take the root square sum
% of these two
a = 311.286; b = 31539.04; c = -0.277426;
FWHM_T = a*sqrt((2.4264e12*(T.^1.5).*exp(-6995.35963./T) + c.*T + 2.0074*5.19e3)) -
b;

% Then the RSS:
FWHM_line = sqrt(FWHM_en.^2 + FWHM_T.^2);
% Also useful to calculate from the FWHM the sigma of the Gaussian; the
% formula is FWHM_line = 2*sqrt(2*log(2))*sigma, so that
sigma_line= FWHM_line./(2*sqrt(2*log(2)));

% Now generate the Gaussians over the range of interest;
E_range = linspace(min(spectIDs.energy),max(spectIDs.energy),5000);
detector_count = zeros(1,length(E_range));
for i = 1:length(lines_of_interest)
        detector_count = detector_count + ...
                lines_to_probe.intensity(i).*exp(-(E_range -
        lines_to_probe.energy(i)).^2./(2*sigma_line(i).^2));
end

semilogy(E_range,detector_count,'r','LineWidth',2)
ylim([min(total_intensity) 10*max(total_intensity)])

% We now desire to determine the contamination between the lines of
% interest and the baseline line defined at the top; first, calculate the
% baseline line ratios for the perfect casesi

baseline_ratios = zeros(1,length(lines_of_interest));

% Determine intensity, energy, and sigma of baseline element in ideal case
baseline_intensity = 0;
E_baseline = 0;
sigma_baseline = 0;
for i = 1:length(lines_of_interest)
        if strcmp(baseline_element,lines_of_interest(i)) == 1
                baseline_intensity = lines_to_probe.intensity(i);
                E_baseline = lines_to_probe.energy(i);
                sigma_baseline = sigma_line(i);
        end
end

% Determine baseline ratios against which to compare later
for i = 1:length(lines_of_interest)
        if strcmp(baseline_element,lines_to_probe.elName(i)) == 0
```

```
            baseline_ratios(i) = lines_to_probe.intensity(i)./baseline_intensity;
      end
end

% This array gives the limits of integration for counts centered around the
% energy center. The first column is the min, the second column is the max,
% the third column is the min index, and the fourth column is the max index

integration_limits = zeros(4,length(lines_of_interest));

for i = 1:length(lines_of_interest)
      integration_limits(i,1) = lines_to_probe.energy(i) - FWHM_line(i)/2;
      integration_limits(i,2) = lines_to_probe.energy(i) + FWHM_line(i)/2;
      integration_limits(i,3) = indexFind(lines_to_probe.energy(i) - FWHM_line
(i)/2,E_range);
      integration_limits(i,4) = indexFind(lines_to_probe.energy(i) + FWHM_line
(i)/2,E_range);
end
% Resize due to peculiarities in the indexFind function
integration_limits = integration_limits(1:length(lines_of_interest),1:4);

% Baseline range: get the integration limits for the baseline
baseline_range = zeros(4,1);
for i = 1:length(lines_of_interest)
      if strcmp(baseline_element,lines_to_probe.elName(i)) == 1
            baseline_range = integration_limits(i,:);
      end
end

% We also define the baseline line distribution
i_baseline = baseline_intensity*exp(-(E_range - E_baseline).^2./
(2*sigma_baseline^2));


% And those of all lines
intensities = zeros(length(lines_of_interest),length(E_range));
for i = 1:length(lines_of_interest)
      intensities(i,:) = ...
            lines_to_probe.intensity(i).*exp(-(E_range -
      lines_to_probe.energy(i)).^2./(2*sigma_line(i).^2));
end

% Calculate ratios of interest for each line of interest against the
% baseline (excluding the baseline, of course)
% The first column in this array is the ratio against the baseline of
% counts with contamination; the second column is the counts of the line in
% its region; the third column is the counts of the baseline in the line
% region; the fourth column is the counts of the line in the baseline
% region; and the fifth column is the coutns of the baseline in the
% baseline region. We have
% C(1) = [C(2) + C(3)]/[C(4) + C(5)]
% The sixth column eta is the accuracy: baseline_ratios(i)/C1 - 1;
% The sixth column eta is the accuracy: (C1 - baseline_ratios(i))/baseline_ratios(i)

ratios_of_interest = zeros(length(lines_of_interest),6);

% Begin loop to calculate lines with contamination
for i = 1:length(lines_of_interest)

% If this line isn't the baseline
      if strcmp(baseline_element,lines_to_probe.elName(i)) == 0
      E1min_index = integration_limits(i,3);
      E1max_index = integration_limits(i,4);
```

```
        E2min_index = baseline_range(3);
        E2max_index = baseline_range(4);
        C2 = sum(intensities(i,E1min_index:E1max_index));
        C3 = sum(i_baseline(E1min_index:E1max_index));
        C4 = sum(intensities(i,E2min_index:E2max_index));
        C5 = sum(i_baseline(E2min_index:E2max_index));
        C1 = (C2 + C3)/(C4 + C5);
        %eta = (C1 - baseline_ratios(i))/baseline_ratios(i);
        eta = baseline_ratios(i)/C1 - 1;
        ratios_of_interest(i,:) = [C1 C2 C3 C4 C5 eta];
        end
end

ratios_of_interest;
```

Summarize the accuracies

```
accuracy_summary = struct('elNamePair',{{}},'accuracy',zeros(1,length
(lines_of_interest)));
for i = 1:length(lines_of_interest)
        if strcmp(baseline_element,lines_to_probe.elName(i)) == 0
                accuracy_summary.elNamePair(i) = strcat(lines_to_probe.elName
(i),'/',baseline_element);% {[lines_to_probe.elName(i),'/',baseline_element]};
                accuracy_summary.accuracy(i) = ratios_of_interest(i,6);
        end
end

accuracy = accuracy_summary;
```

C.2. MATLAB Source Code: run_Spectral_Res_for_Loop

```
%%%%%%%%%%%%%%%%%%%%%%%%%%%%%%%%%%%%%
% Updated spectral resolution loop
%
%      Niraj Inamdar
%             15 January 2013
%%%%%%%%%%%%%%%%%%%%%%%%%%%%%%%%%%%%%%
temperature = 273 + linspace(-70,-50,300);
eta = .1;
%accs = zeros(1,length(temperature));
MgSi = zeros(1,length(temperature));
AlSi = zeros(1,length(temperature));
SSi = zeros(1,length(temperature));

for i = 1:length(temperature)
accs = Updated_Spectral_Res_for_Loop(temperature(i));
MgSi(i) = accs.accuracy(1);
AlSi(i) = accs.accuracy(2);
SSi(i) = accs.accuracy(4);
end


spectIDs = spectID_info;

accs = Updated_Spectral_Res_for_Loop(temperature(i));


figure
semilogy(temperature - 273,abs(MgSi),'r*','LineWidth',1)
hold on
semilogy(temperature - 273,abs(AlSi),'g*','LineWidth',1)
semilogy(temperature - 273,abs(SSi),'b*','LineWidth',1)
hline(eta,'m')
%hline(-.1,'m')
%grid on


xlab = xlabel('Detector temperature
[C]','FontName','TimesNewRoman','FontSize',18,'Interpreter','Latex');
ylab = ylabel('Line measurement
accuracy','FontName','TimesNewRoman','FontSize',18,'Interpreter','Latex');
leg = legend('Mg/Si','Al/Si','S/Si');
head = title('Line measurement accuracy as a function of
temperature','FontName','TimesNewRoman','FontSize',18,'Interpreter','Latex');
set(xlab,'Interpreter','Latex');
set(ylab,'Interpreter','Latex');
set(head,'Interpreter','Latex');
set(leg, 'Interpreter', 'Latex');
%ti_thing = sprintf('Equilibrium time as a function of force coefficient \gamma for
various $b$ and $k$');
set(gca, 'FontName', 'Times New Roman', 'FontSize', 18);


%MgSiIndex = indexFind(0,MgSi-eta);
%vline(temperature(MgSiIndex)-273);
vline(zeroSearch_Simp(temperature,MgSi-eta) - 273,'r')
```

C.3. MATLAB Source Code: spectIDs

```
%%%%%%%%%%%%%%%%%%%%%%%%%%%%%%%%%%%%%
%
% Updated spectral resolution code
%
%      Niraj Inamdar
%            15 January 2013
%
%%%%%%%%%%%%%%%%%%%%%%%%%%%%%%%%%%%%%%
% Set energy rang we're interested in probing
E_min = .65; %In keV
E_max = 2.5; %In keV


spectralLines = spectIDs;
```